SIMULATING ACOUSTIC WAVE REFLECTION, TRANSMISSION, AND SCATTERING IN K-WAVE FOR QUANTITATIVE ULTRASOUND APPLICATIONS

BY

KARTHIK JEDIKERE NAGABHUSHANA

THESIS

Submitted in partial fulfillment of the requirements
for the degree of Master of Science in Electrical and Computer Engineering
in the Graduate College of the
University of Illinois Urbana-Champaign, 2021

Urbana, Illinois

Adviser:

Research Assistant Professor Aiguo Han

ABSTRACT

K-Wave is a versatile and powerful acoustic simulator that has gained popularity in the Medical Ultrasound research community. In this work, k-Wave was used to model two quantitative ultrasound (QUS) applications.

In Part 1, detailed in Chapter 3, acoustic planar reflection and transmission were simulated to validate a new phantom attenuation measurement method. Attenuation coefficient (AC) measurements of reference phantoms, a key step in quantitative ultrasound, are complicated by transmission loss of laminate membranes. Conventional through-transmission methods overcome this issue by characterizing separately membrane and phantom material specimens. A simpler alternative that uses a single phantom to simultaneously measure the membrane transmission loss and phantom material AC is proposed. The proposed method was validated in simulation using the k-Wave toolbox. The acquired AC, between 0.5-1 dB/cm-MHz, had a maximum error of 0.06 dB/cm-MHz. The method was also experimentally validated wherein AC measurements were performed by two operators on five distinct phantoms, across five transducers, using the conventional method and the proposed method. The acquired AC, between 0.28-1.48 dB/cm-MHz, had a maximum error of 0.045 dB/cm-MHz across all phantoms.

In Part 2, detailed in Chapters 4-6, acoustic scattering was simulated in k-Wave to extract backscattering parameters. This exercise was intended to be a precursor to a simulation of tissue histology-based computational phantoms known as 3D impedance maps (3DZMs) in k-Wave. In the past, 3DZM simulations have either used the spatial FFT approach or semi-analytical tools such as Field-II. However, both methods assume plane wave incidence, weak scattering, and the absence of multiple scattering in their analysis which is a limitation. A simulation in k-Wave transcends these assumptions and hence fulfills the full potential of a 3DZM. First, three schemes– *focused transducer*, *near-field*, and *far-field* were implemented in k-Wave to extract the differential backscatter cross-section of a 1-mm single fluid spherical scatterer. Planar reference method [1] with a single element spherically focused transducer was implemented in the *focused transducer* scheme. In the *near-field* scheme, the single scatterer was placed in the near-field of a

wide planar transmitter and a point receiver was placed in the far-field. In the *far-field* scheme, the single scatterer was placed in the far-field of a piston transmitter and a point receiver was placed in the far-field. For a spatial resolution of 25 μm and within a frequency bandwidth of 1 to 3.5 MHz, the extracted differential backscatter cross-section's root mean square (RMS) error was within 12.2%, 3.2%, and 3.4% of the peak value for the *focused transducer*, the *near-field*, and the *far-field* schemes respectively. Next, the backscatter coefficient (BSC) of a sparsely distributed collection of identical 20 μm fluid spherical scatterers was extracted in a radially averaged manner from a 192 μm wide spherical scattering volume. The extracted BSC was found to be a product of the single scatterer BSC and the number of scatterers in the same volume, thus matching the incoherent scattering theory. Finally, a staircase-free representation of the non-rectangular sources from the literature was successfully extended to heterogeneous simulation media, both for the single scatterer and the scatterer collection. For a spatial resolution of 100 μm and within a frequency bandwidth of 1 to 3.5 MHz, the extracted differential backscatter cross-section of a single 1 mm fluid spherical scatterer had an RMS error of 90.1% of the peak value. In contrast, the staircase-free version had an RMS error of 10.8% of the peak value. Overall, this work successfully set up a simulation flow to model backscattering in k-Wave, which can be extended to 3DZMs.

ACKNOWLEDGEMENTS

This work was made possible by the generosity of many people. First and foremost, I want to thank my research advisor, Dr. Aiguo Han, for his constant support, encouragement, and mentorship. His vision and foresight helped me immensely in finding worthwhile problems and in pursuing them systematically. I also want to convey my heartfelt gratitude to Dr. William D. O'Brien, Jr. for guiding and challenging me to be a better researcher and communicator. His feedback was invaluable in bringing clarity and depth in my research.

I am also very grateful to Dr. Rita J. Miller for training and supporting me in my experimental work. Additionally, I must acknowledge the efforts of Qiuyu Wang in the phantom attenuation experiments. I must also thank my colleagues and fellow researchers in the Bioacoustics Research Laboratory for many helpful discussions.

The simulation-based work made use of the Illinois Campus Cluster, a computing resource that is operated by the Illinois Campus Cluster Program, and the HAL-DGX A100 server maintained by the Innovative Systems Lab at the National Center for Supercomputing Applications. I would like to express my gratitude to Dr. Volodymyr Kindratenko, Dr. Dawei Mu, and everyone else who made this collaboration possible.

Finally, I want to thank my parents for their love and affection. I am also deeply grateful to my wife, Ananya, for being my source of strength and happiness. With her, an uncertain and challenging journey became exciting and joyous.

TABLE OF CONTENTS

LIST OF ABBREVIATIONS

1D	One-dimensional
2D	Two-dimensional
3D	Three-dimensional
3DZM	Three-dimensional impedance map
BSC	Backscatter coefficient
CPU	Computer Processing Unit
FFT	Fast Fourier Transform
GPU	Graphics Processing Unit
QUS	Quantitative Ultrasound
RMS	Root mean square
SF	Structure Function

CHAPTER 1
AN OVERVIEW OF ACOUSTIC WAVE SIMULATORS

Acoustic wave simulators play an important role in medical ultrasound research. Common applications are: 1) Visualization of beam patterns in the design of new transducers, which is essential in iterative and fast design cycles [2], [3]. 2) Design and validation of new excitation and post-processing schemes. Since the medium properties can be controlled in the simulators, such schemes can be validated by comparing the acquired qualitative images and quantitative parameters with the ground truth. 3) Real-time clinical applications such as treatment planning in high intensity focused ultrasound (HIFU) [4], [5], and ultrasonic brain therapy [6]. 4) In quantitative ultrasound (QUS) to simulate scattering intensity [7], scattering statistics [8], and attenuation [9], [10]. Such simulations help choose appropriate statistical models, better post-processing strategies, and in incorporating complexities such as transducer diffraction and medium attenuation. In the future, these simulations can also help in the design of tissue-specific transducer and excitation schemes, and in generating training data for QUS-specific neural networks. In addition, this work focuses on acoustic simulations in QUS applications.

Over the years, many simulators have been used such as Field II, FOCUS, INCS, and k-Wave for different applications [11]. However, Field II and k-Wave are the most popular based on an analysis of the citations in academic journals [12]. Between the two, k-Wave is the more versatile and complete tool. Hence, k-Wave was used in this work to validate a novel phantom attenuation measurement method, and to model the acoustic backscatter from single scatterers and a collection of scatterers. A systematic procedure to model and extract acoustic backscatter in k-Wave does not exist in the literature. Hence the backscatter modeling exercise in k-Wave would be a valuable addition to the literature.

Field II was developed in the 1990s by Jensen [13]–[15]. It supports linear longitudinal wave propagation in a homogenous medium with point scatterers and no multiple scattering. Then, the overall field pattern and the received echoes are calculated using the spatial impulse response method of Tupholme [11] and Stepanishen [12]. The tool was written in C for the MATLAB

platform. It has built-in functions for implementing various transducer types (single element and arrays) and functions (focusing and apodization), and example codes to implement computational phantoms. However, Field II does not support many important acoustic phenomena such as reflection, transmission, and scattering from arbitrary shapes, nonlinear wave propagation, and elastic wave propagation, among others. This limits its use in key medical ultrasound modalities such as harmonic imaging, quantitative ultrasound (QUS), and elastography, Besides, only an attenuation model linear with frequency is supported. Furthermore, while the code is free, it is not open source. However, it is easy to use and has fast simulation times. Hence, despite its limitations, it is a popular tool to simulate B-mode imaging and blood flow imaging.

Introduced by Treeby et al. in 2010 [18], k-Wave is one of the most versatile acoustic simulators. Built for MATLAB, it supports medium heterogeneity, power-law absorption, nonlinear wave propagation [19], and elastic wave propagation [20]. Unlike Field II, it is a *full-wave method* since it directly solves the underlying acoustic equations without any analytical approximations. This, however, increases the computational complexity in terms of memory requirement and simulation time. But recent advances in computing power have made such large and complex simulations feasible. Moreover, k-Wave uses a computationally efficient pseudo-spectral method for solving acoustic equations. In addition, each simulation involves several FFTs that can be parallelized. Indeed, the GPU-based and cluster-based parallel implementations of k-Wave are extremely fast [21], [22]. Furthermore, with functions to simulate thermal diffusion, perform photoacoustic reconstruction and implement the angular spectrum method, it is the most complete package compared to its competition. Finally, it is free, has an open-source code, and possesses a vibrant user community that makes it a compelling choice for medical ultrasound research.

CHAPTER 2
INTRODUCTION TO K-WAVE

This work utilized k-Wave for simulating longitudinal linear acoustic wave propagation in a heterogeneous and attenuative medium. This chapter will first introduce the governing differential equations for such a wave and its implementation in k-Wave. Next, it will discuss the design of the simulation setup. Finally, it will conclude with the finer aspects of k-Wave such as stability, accuracy, numerical dispersion, and aliasing. In summary, portions from the k-Wave user manual [23] relevant to this work are discussed in this chapter.

2.1 Acoustic wave equations and their implementation in k-Wave

The generalized discrete Westerwelt wave equation is implemented in k-Wave [19]. For linear wave propagation in an attenuative medium, this equation is expressed as given in Equations (2.1) – (2.3). The equations for momentum conservation, mass conservation, and pressure-density relation are given by, respectively,

$$\frac{\partial \boldsymbol{u}}{\partial t} = -\frac{1}{\rho_0}\nabla p + \boldsymbol{S_F}\ , \tag{2.1}$$

$$\frac{\partial \rho}{\partial t} = -\rho_0 \nabla \cdot \boldsymbol{u} + S_M\ , \tag{2.2}$$

$$p = c_0^2(\rho - \mathrm{L}\rho)\ , \tag{2.3}$$

where $\boldsymbol{u}$ is the particle velocity vector, p is the acoustic pressure, and ρ is the acoustic density. Next, ρ_0 is the ambient density and c_0 is the sound speed, both of which are defined by the user for the heterogeneous computational domain. $\boldsymbol{S_F}$ is the force source vector and represents the input of body forces per unit mass. S_M is the mass source term and represents the time rate of the input of the mass per unit volume. The transducer elements can be either defined as a mass source or a force source. Then, the user-defined time-domain excitation signal will be proportional to either S_M or $\boldsymbol{S_F}$. In this study, however, the transducer elements were always defined as mass sources.

Operator L is linear integrodifferential and accounts for acoustic absorption and dispersion that supports a frequency power law.

Now, a spatially and temporally discretized version of Equations (2.1) – (2.3) is implemented. Then, starting from the initial conditions set by the user, the state of the entire domain is calculated for each time step. For illustration, in a linear non-attenuative 3D domain, the discrete equations for the x-axis are given by

$$\frac{\partial}{\partial x} p^n = \mathcal{F}^{-1}\left\{ ik_x \kappa e^{ik_x \Delta x/2} \mathcal{F}\{p^n\} \right\}, \tag{2.4}$$

$$u_x^{n+1/2} = u_x^{n-1/2} - \frac{\Delta t}{\rho_0} \frac{\partial}{\partial x} p^n + \Delta t \, S_{F_x}^n \,, \tag{2.5}$$

$$\frac{\partial}{\partial x} u_x^{n+1/2} = \mathcal{F}^{-1}\left\{ ik_x \kappa e^{-ik_x \Delta x/2} \mathcal{F}\{u_x^{n+1/2}\} \right\}, \tag{2.6}$$

$$\rho_x^{n+1} = \rho_x^n - \frac{\Delta t}{\rho_0} \frac{\partial}{\partial x} u_x^{n+1/2} + \Delta t \, S_{M_x}^{n+1/2} \,, \tag{2.7}$$

where $\mathcal{F}$ is the Fourier operator, $\mathcal{F}^{-1}$ is the inverse Fourier operator, Δt is the user-defined time step, and Δx is the user-defined grid spacing. The superscript n indicates nth time step for state variables p and ∇p, and the fractional time steps such as $n + 1/2$ indicate a staggered temporal representation for the state variables $\boldsymbol{u}$ and $\nabla \cdot \boldsymbol{u}$. Additionally, compared to the state variables p and $\nabla \cdot \boldsymbol{u}$, the state variables $\boldsymbol{u}$ and ∇p are also spatially staggered by half a step in all dimensions. This spatial shift in the x-direction is realized by multiplying $e^{ik_x \Delta x/2}$ or $e^{-ik_x \Delta x/2}$ terms with the state variables represented in the spatial frequency domain. Finally, $\boldsymbol{k}$ is the spatial frequency (or wavenumber) and κ is the k-space correction factor to counteract the finite difference approximation of the temporal derivative given as

$$\kappa = sinc(c_{ref} k \Delta t/2) \,, \tag{2.8}$$

where c_{ref} is a reference sound speed that should be suitably chosen as discussed later in this chapter. The state variables (p, $\boldsymbol{u}$, ∇p, ρ, and $\nabla . \boldsymbol{u}$) are defined for the entire domain (a 3D grid in this case). Then, Equations (2.4) and (2.6) calculate spatial gradient using the FFT and IFFT (3D-FFT and 3D-IFFT in this case) to the state variables. This use of discrete spectral points for modeling and analysis of objects is known as Fourier collocation. Next, Equations (2.5) and (2.6)

update the state variables based on the first-order forward difference method. Thus, a spectral approach is adopted for spatial stepping and a finite-difference approach is adopted for temporal stepping in the wave equation.

2.2 Simulation setup in k-Wave

A simulation setup in k-Wave will need three fundamental components—*medium*, *source*, and *sensor*. The user can define a heterogenous distribution of acoustic properties (sound speed, ambient density, attenuation coefficient, B/A non-linear parameter) over the entire computational domain by defining the *medium* object. The *medium* object also encapsulates common simulation parameters such as the grid step (dx), time step (dt), and simulation end time. For non-attenuative media, the attenuation coefficient must be set to 0. For linear wave propagation, the B/A parameter must be left undefined. Although the grid spacing in each dimension can be different, in this study, they were set to be the same.

Next, the *source* object is the input or excitation that generates acoustic waves in the domain. Any arbitrary and discontinuous shape in the domain can be defined as the source. Subsequently, independent excitation signals can also be defined for each point on the source map. The excitation can either be a pressure scalar corresponding to a mass source, or a particle velocity vector corresponding to a force source. Also, the excitation can either be additive or set as a Dirichlet boundary condition. In this study, however, additive mass sources were used. Then, for a pressure excitation signal $p_{in}(t)$, the mass source term for x-dimension was internally defined by k-Wave as

$$S_{M_x} = \frac{p_{in}(t)}{N c_0} \frac{2}{dx}, \tag{2.9}$$

where N is the number of dimensions of the domain. Although S_M is a scalar, it is split along the x, y, and z dimensions (for a 3D case) for numerical implementation. Then, by combining Equations (2.1) – (2.3), the continuous wave equation for the simulation is given by

$$\nabla^2 p - \frac{1}{c_0^2} \frac{\partial^2 p}{\partial t^2} = -\frac{\partial}{\partial t} S_M \, . \tag{2.10}$$

The pressure excitation in the simulation was chosen to be a sinusoid with a Gaussian envelope. The Gaussian excitation was intended to mimic the electro-mechanical transfer functions of commonly available single-element transducers. Additionally, the Gaussian envelope ensured that the excitation signal was compact in the time domain and the frequency domain. Pulse-echo imaging was implemented in this work and hence temporal compactness was necessary to resolve echoes from different surfaces or objects. Since k-Wave followed an FFT-based approach to compute spatial gradients, the spectral support was finite. Hence, spectral compactness was also desirable. However, any excitation that is compact in time and frequency was sufficient for this work. The Gaussian excitation was chosen due to its simplicity and familiarity. Consequently, the excitation term in the wave equation, $\frac{\partial}{\partial t} S_M$, was set to be a Gaussian sinusoid.

Next, the *sensor* object defines the positions for sensing and acoustic state variables (p or $\boldsymbol{u}$) to be recorded in the domain. Like the *source* object, any arbitrary and discontinuous shape in the domain can be defined as a sensor. In this study, the pressure state variables were recorded. In k-Wave, the output measured on the sensor is temporally staggered by half time step compared to the input state variable. However, there was no spatial staggering between the input and output.

The complete transmit-receive signal chain is shown in Fig. 2.1 where an impulse electrical input to the transmitter generated a Gaussian sinusoidal acoustical excitation signal. The center frequency of the excitation was f_c and σ was related to the -3 dB bandwidth BW as $\sigma = BW/2\sqrt{\ln 2}$. G_{tx} was the transmit gain in Pa/V and G_{rx} is the receive gain in V/Pa. An integral operator was placed in the signal chain to counteract the time-differentiation as outlined in Eq. (2.10). The receiver impulse response was also defined to be a Gaussian sinusoid to mimic commonly available single-element transducers.

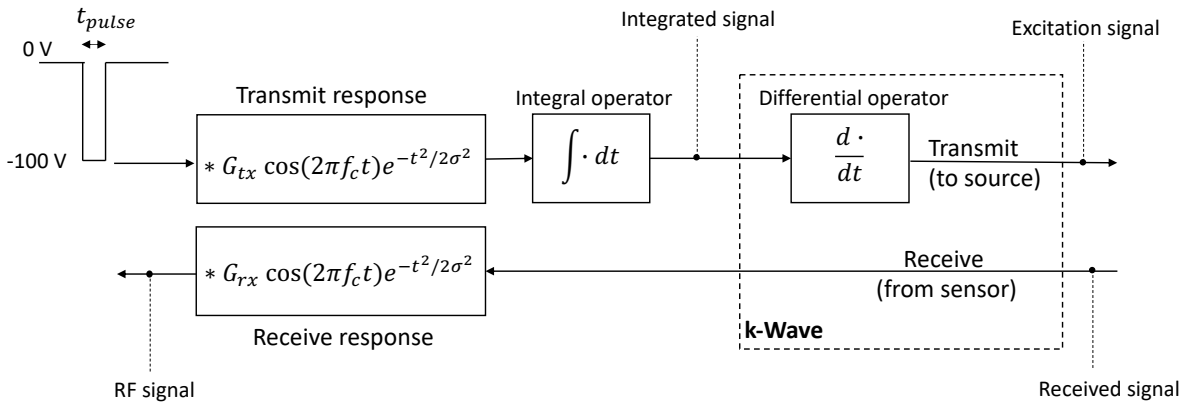

Fig. 2.1. Transmit-receive signal chain used in the k-Wave simulations

To illustrate transmit-receive operation, the signals marked in Fig. 2.1 are plotted in Figs. 2.2 and 2.3 for the following settings: f_c = 2.25 MHz, -3 dB bandwidth = 50%, G_{tx} = 10^4 Pa/V, and G_{rx} = 10^{-6} V/Pa.

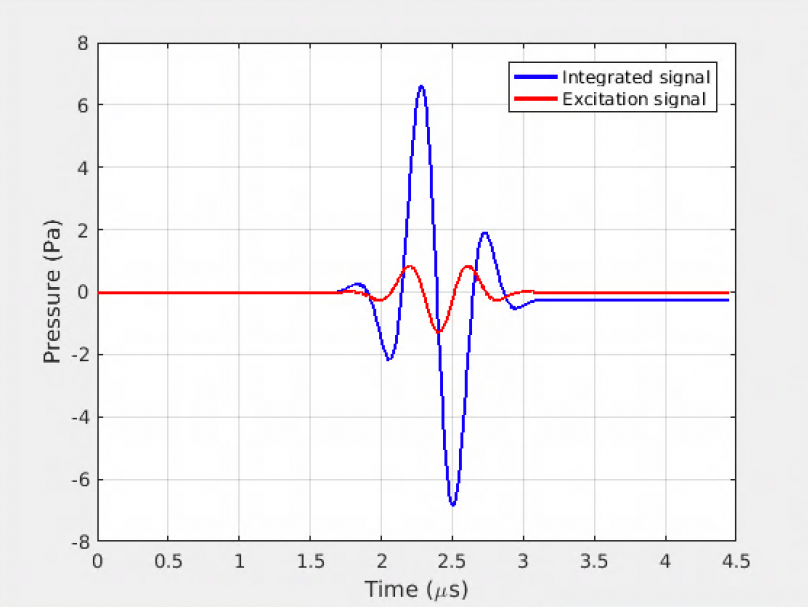

Fig. 2.2. Signals in the transmit signal chain. The excitation signal is directly applied on all the source points along the surface of the transmitter.

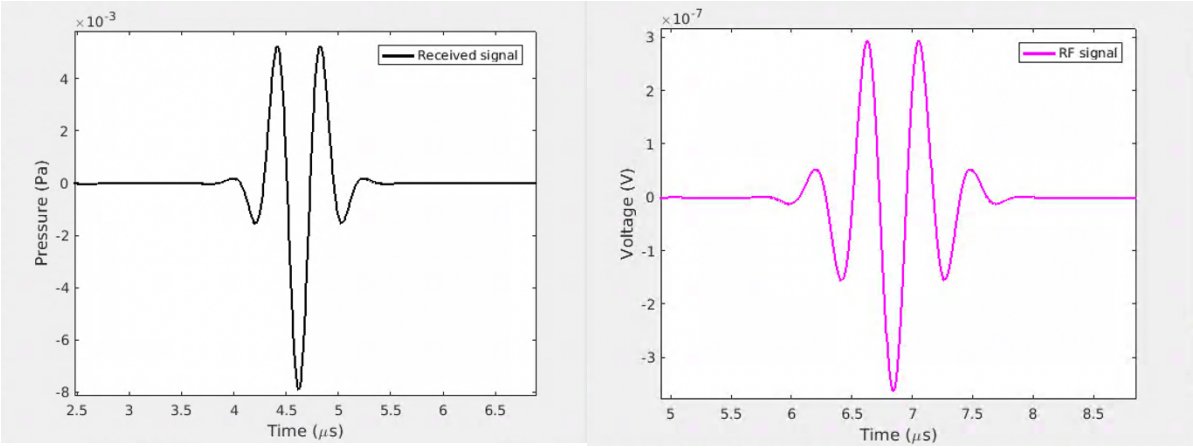

Fig. 2.3. Signals in the receive signal chain for a single sensor point. If the receiver has more than one point, a summation of the RF signals from all the points along receiver surface is considered.

2.3 Miscellaneous simulation settings

Spatial and temporal discretization in k-Wave, respectively, induces spatial and temporal aliasing that must be minimized to ensure simulation accuracy. Between the two, spatial aliasing is the more dominant effect in k-Wave. For a grid spacing of dx, the spatial Nyquist is given by $k_{Nyquist,spatial} = 0.5/dx$. Similarly, the temporal Nyquist frequency is given by $f_{Nyquist,temporal} = 0.5/dt$. By default, k-Wave spatially smoothens the medium with a -3 dB cut-off spatial frequency of $0.67k_{Nyquist,spatial}$. In this study, the pressure excitation signal was also filtered with a -3 dB cut-off frequency $f_{cut} = 0.67 \min\{c_0\} k_{Nyquist,spatial}$, as recommended by the k-Wave manual [23].

Alternatively, points per wavelength (PPW) and points per period (PPP), are also used to quantify the spatial and temporal aliasing respectively. For a wavelength of λ, $PPW = \lambda/dx$ and $PPP = \lambda/c_0/dt$. Then, the spatial Nyquist and temporal Nyquist can also be represented as $2\,PPW$ and $2\,PPP$ respectively. Next, the ratio PPW/PPP is known as the Courant-Friedrichs-Lewy (CFL) number. To ensure simulation stability of a heterogeneous medium, the CFL given as

$$CFL = \frac{PPW}{PPP} = \frac{dt}{dx}\max\{c_0\}, \tag{2.11}$$

must be lower than 0.3. In this study, a CFL of 0.25 was used unless specified otherwise. In addition, the k-space operator κ introduces some additional stability constraints on c_0 (sound speed map) and c_{ref} (reference sound speed) for heterogeneous media given by

$$c_{ref} < c_0 \text{ , and} \tag{2.12}$$

$$CFL < \frac{2}{\pi}\left(\frac{c_0}{c_{ref}}\right)\sin^{-1}\left(\frac{c_{ref}}{c_0}\right). \tag{2.13}$$

The reference speed in this work was set to be the sound speed of background water which was 1480 m/s.

Due to the use of Fourier spectral collocation, k-Wave is best suited for smooth variations in the medium properties. Modeling steep spatial steps is challenging and requires high spatial sampling (or low dx), resulting in large domains. Often, memory requirements for such domains can be prohibitively large and result in long simulation run times. For a given frequency bandwidth, this necessitates a trade-off between spatial resolution and computational resources. Right grid spacing for an abrupt spatial step depends on the step magnitude, bandwidth of interest, and application. Consequently, a preliminary iterative process must be followed to decide the grid spacing for a given application discussed in more detail in Chapter 3.

To carry out free-space simulations in a finite domain, k-Wave offers a feature known as a perfectly matched layer (PML). The use of spatial FFTs in k-Wave implies that the wave field is spatially periodic. This implication causes waves leaving from one edge of the domain to reappear at the opposite edge. This effect is minimized by placing a hypothetical perfectly matched layer on the edges of the domain that attenuates outward going waves while minimizing reflections. A PML width of 20 grid points was used in this study. For perpendicular incidence, a 20-grid-point PML provided a transmission coefficient of -70 dB and a reflection coefficient of -100 dB in the bandwidth of interest (PPW > 3) [24].

Finally, single (4 bytes) precision was used for simulations and for recording output waveforms. This precision gave a signal to quantization noise ratio of -140 dBc/Hz, which was adequate in this work. Version 1.1 of k-Wave was used for the work presented in Chapter 3 whereas Version 1.3 was used for the work discussed in Chapters 4-6. For the 3D simulations,

CPU-based C++ code was used for Chapter 3 and GPU-based C++ code was used for simulations in Chapters 4-6. The axisymmetric simulations presented in Chapter 4 were performed in MATLAB.

CHAPTER 3
DESIGN OF A NEW PULSE-ECHO TECHNIQUE TO MEASURE PHANTOM ULTRASONIC ATTENUATION COEFFICIENT, AND VALIDATION IN K-WAVE AND EXPERIMENTS

3.1 Introduction

Phantoms are widely used in clinical ultrasound research for testing and validation. They are even more important in quantitative ultrasound (QUS) applications requiring calibrated reference phantoms to correct transducer diffraction [1]. To standardize QUS methods, it is critical to characterize the phantom material sound speed, AC, and BSC accurately and precisely. A phantom is composed of tissue-mimicking materials that acoustically mimic biological media. The phantom material is housed in a supportive casing, and the outer surfaces are lined with protective membranes for ease of use in clinical settings. Typical use has the phantom immersed in water (Fig. 3.1). The phantom material is housed in a cylindrical polyvinyl chloride (PVC) casing and is lined with protective membranes on the top and bottom surfaces. The top and bottom membranes are assumed to have the same properties. While the membranes perform the crucial task of isolating the phantom material from external media, they also result in ultrasonic transmission loss for the waves passing through them. Consequently, measurements of phantom material AC (hereafter referred to as phantom AC) must be corrected for membrane transmission loss.

Traditionally, through-transmission techniques have been employed to characterize phantom AC with reasonable accuracy [25], [26]. These techniques measure the insertion loss that represents the combined effects of phantom AC and membrane transmission loss. The techniques require knowledge of membrane transmission loss to derive phantom AC from the insertion-loss measurement. Conventionally, the membrane transmission loss was approximated by elaborate measurements [25]. First, the transmission loss at the water-membrane-water interface was measured using a separate membrane specimen. Second, the mass density, sound speed, and thickness of a typical membrane sample were physically measured over multiple specimens. Third,

the density of the phantom material was physically measured. Additionally, the sound speed and thickness of the phantom material were acoustically measured using a pulse-echo setup. Finally, these measured ultrasonic parameters were combined to estimate the water-membrane-phantom material transmission loss. These methods are cumbersome as they require standalone specimens of membrane and phantom material and additional measurements. Moreover, stand-alone membrane and phantom material may not be available. To address these issues, a method was recently proposed [27] to directly estimate the membrane transmission loss for a given phantom using a single-element transducer in a pulse-echo configuration.

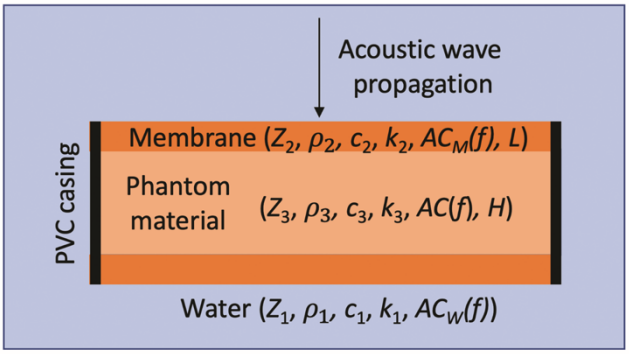

Fig. 3.1. Typical QUS reference phantom (side view). Membrane thickness (L) is much less than phantom thickness (H). For each medium, Z_i indicates acoustic impedance, ρ_i indicates density, c_i indicates sound speed, and k_i indicates wavenumber. Further, $AC_M(f)$, $AC(f)$, and $AC_W(f)$ represent AC in dB/cm-MHz of the membrane material, phantom material, and water, respectively.

The proposed technique estimates the phantom AC without requiring additional membrane samples or prior knowledge of the phantom material and membrane properties. While the conventional method estimates the membrane loss of a typical membrane specimen, the proposed method estimates the membrane loss for the given phantom. Thus, any variation in membrane loss across specimens or within an individual specimen over time can be factored out of phantom AC measurements. Furthermore, this method can be adopted by phantom manufacturers or third-party calibrators as part of their reference phantom calibration strategy that would be necessary for widespread clinical adoption of reference phantom-based QUS applications.

In this chapter, a simulation-based validation of the proposed technique was conducted using k-Wave. Additionally, the technique was experimentally evaluated using different phantoms

and transducers over a range of frequencies (0.7-16 MHz). The chosen frequency range was relevant in typical QUS applications such as in the characterization of the liver (1-6 MHz) [28]–[30], kidney (5-15 MHz) [31], prostate (4-8 MHz) [32], eyes (5-15 MHz) [33], and blood (9-28 MHz) [34]. Finally, the technique's robustness and limitations were analyzed.

3.2. Theory

This section will first introduce the theory of acoustic reflection and transmission for membranes. Then the steps followed to estimate the membrane transmission loss and phantom AC are explained.

3.2.1. Membrane reflection and transmission coefficients

The ultrasonic pressure reflection and transmission coefficients of a thin membrane at normal incidence (Fig. 3.1) are well understood [35]. Let the pressure reflection coefficient for the water-membrane-phantom (WMP) and phantom-membrane-water (PMW) interfaces be R_1 and R_2, respectively. Similarly, let the pressure transmission coefficients for the WMP and PMW interfaces be T_1 and T_2, respectively. Then,

$$R_1(f) = \frac{(Z_3 - Z_1)Z_2 \cos(k_2 L) + j\left(Z_2^2 - Z_3 Z_1\right)\sin(k_2 L)}{(Z_3 + Z_1)Z_2 \cos(k_2 L) + j\left(Z_2^2 + Z_3 Z_1\right)\sin(k_2 L)} \tag{3.1}$$

$$R_2(f) = \frac{(Z_1 - Z_3)Z_2 \cos(k_2 L) + j\left(Z_2^2 - Z_1 Z_3\right)\sin(k_2 L)}{(Z_1 + Z_3)Z_2 \cos(k_2 L) + j\left(Z_2^2 + Z_1 Z_3\right)\sin(k_2 L)} \tag{3.2}$$

$$T_1(f) = \frac{2\, Z_3 Z_2}{(Z_3 + Z_1)Z_2 \cos(k_2 L) + j\left(Z_2^2 + Z_3 Z_1\right)\sin(k_2 L)} \tag{3.3}$$

$$T_2(f) = \frac{2\, Z_1 Z_2}{(Z_1 + Z_3)Z_2 \cos(k_2 L) + j\left(Z_2^2 + Z_1 Z_3\right)\sin(k_2 L)} \tag{3.4}$$

$$k_2 = \frac{2\pi f}{c_2} \tag{3.5}$$

The membrane is reasonably assumed to be nonattenuative ($AC_M(f) = 0$) for which the wavenumber (k_2) is a real number. To compensate for the membrane transmission loss in the phantom AC measurements, all the parameters listed in Eq. (3.1) – (3.5) must be known or

estimated. Water's acoustic impedance (Z_1) can be calculated using the water temperature [36]. But other parameters are unknown and must be estimated.

3.2.2. Measurement steps

The measurement setup employs a single-element transducer arranged in a pulse-echo configuration (Fig. 3.2). The surface of interest is placed at the planar focus at a distance, D, from the transducer, for all setups. The planar focus is determined by moving the planar reference surface (i.e., Plexiglas) to maximize the echo amplitude.

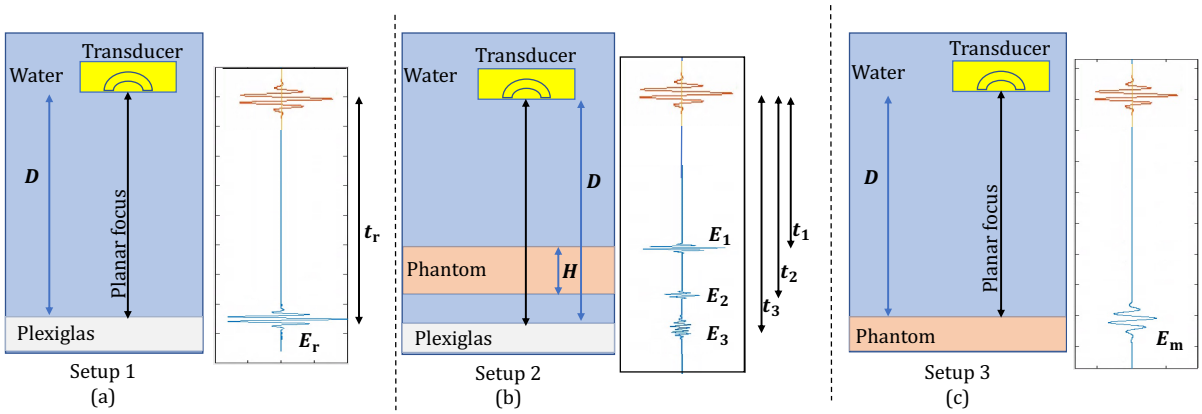

Fig. 3.2. Proposed technique pulse-echo setups for measuring phantom AC.

3.2.2.1. Measuring phantom insertion loss

The phantom insertion loss is measured using setups 1 and 2 (Fig. 3.2). First, the reference echo, E_r, is acquired from the Plexiglas surface placed at the transducer focus, without phantom insertion (Setup 1; Fig. 3.2(a)). Next, the phantom specimen is inserted between Plexiglas and transducer (Setup 2; Fig. 3.2(b)) to acquire echoes E_1, E_2, and E_3 from the phantom top, bottom, and Plexiglas surfaces, respectively. Echo E_3, denoted the attenuation echo, is used along with E_r to calculate the phantom insertion loss from

$$Insertion\ Loss(f) = 20\log_{10}\left(\frac{E_r(f)}{E_3(f)}\right) \tag{3.6a}$$

The phantom insertion loss is expressed in terms of the phantom AC and membrane transmission coefficients using

$$20\log_{10}\left(\frac{E_r(f)}{E_3(f)}\right) = 2fH[AC(f) - AC_w(f)] - 20\log_{10}|T_1(f)T_2(f)|^2, \quad (3.6b)$$

where $AC(f)$ is the frequency-dependent AC (in dB/cm-MHz) of the phantom material, f is the frequency (in MHz) and H is the phantom thickness (in cm). $AC_W(f)$ is the frequency-dependent AC (in dB/cm-MHz) of the water determined using the temperature (τ, in degree Celsius) [37] as

$$AC_W(f) = (1 - 3.84\times10^{-4})\cdot(55.9 - 2.37\tau + 4.77\times10^{-2}\tau^2 - 3.48\times10^{-4}\tau^3)\cdot10^{-5}$$
$$\cdot(20\log_{10} e)\cdot f^2. \quad (3.7)$$

$[T_1(f)T_2(f)]^2$ is the round-trip pressure transmission coefficient caused by the membrane expressed as

$$T_{roundtrip}(f) = [T_1(f)T_2(f)]^2\ . \quad (3.8)$$

$AC(f)$ can be obtained from Eq. (3.6b) if $|T_{roundtrip}(f)|$ and H are known, which are estimated in the subsequent steps.

3.2.2.2. Estimating round-trip membrane transmission coefficient

Membrane echo, E_m, is recorded by placing the phantom top surface with the membrane at the planar focus (Setup 3; Fig. 3.2(c)). The magnitude of the WMP reflection coefficient $R_1(f)$ is estimated by

$$|R_1(f)| = |R_{plexi}|\cdot\frac{|E_m(f)|}{|E_r(f)|}, \quad (3.9)$$

where the water-Plexiglas reflection coefficient, R_{plexi}, is 0.375 based on the Plexiglas sound speed of 2758 m/s and density of 1180 (kg/m^3) [38], [39]. $|T_{roundtrip}(f)|$ is then estimated from $|R_1(f)|$ using the procedure shown in Fig. 3.3. Specifically, Eq. (3.1) is fitted to the membrane reflection coefficient, $|R_1(f)|$, to estimate the unknown parameters Z_2, Z_3, and L/c_2. Prior knowledge of the phantom that the acoustic impedance of the membrane and the phantom material

are greater than those of the water is used during the least square fit. Finally, the estimated unknown parameters are substituted in Eq. (3.3) and (3.4) to estimate $|T_1(f)T_2(f)|$, leading to $|T_{roundtrip}|$ as shown in Fig. 3.3.

In this analysis, ultrasonic waves at the planar focus are assumed to be planar, a good approximation for weakly focused single-element transducers commonly used in QUS applications [40]. During estimation, it was assumed that Z_2 and Z_3 lie between 0.75 and 15 MRayl. It was also assumed that the ratio L/c_2 ranged between 0.2 ns and 1 μs.

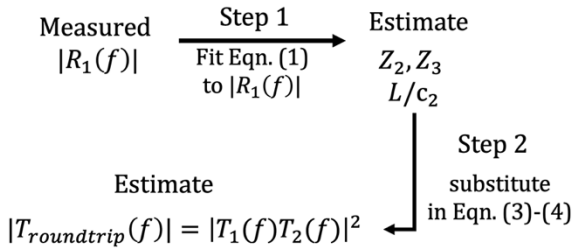

Fig. 3.3. Procedure for estimating the magnitude of round-trip transmission coefficient ($|T_{roundtrip}(f)|$).

3.2.2.3. Estimating phantom thickness

The phantom thickness H is estimated by using the echoes obtained from setups 1 and 2. A time of flight analysis yields

$$H = \frac{c_1}{2} \cdot ((t_r - t_3) - (t_r - t_2) + (t_r - t_1)), \tag{3.10}$$

where the sound speed in water, c_1, is known, and the time differences $t_r - t_3$, $t_r - t_2$, and $t_r - t_1$ are obtained from the echoes using cross-correlation.

3.2.2.4. Processing phantom attenuation coefficient

Finally, the estimated round-trip membrane transmission loss and measured phantom thickness are resubstituted into Eq. (3.6a) and (3.6b) to estimate the phantom attenuation coefficient, $AC(f)$, by

$$AC(f) = AC_w(f) + \frac{1}{2fH} Insertion\ Loss + \frac{1}{2fH} 20 \log_{10} |T_{roundtrip}(f)| \quad (3.11)$$

3.3. Simulation-based validation in k-Wave

The proposed phantom attenuation measurement technique was applied on a simulated phantom in k-Wave. The simulation-acquired AC results were compared with the predefined attenuation profile of the phantom to validate the technique.

3.3.1 Setup

Implementation of the proposed technique was split across three setups. Each of the three setups included the transducer, phantom, and Plexiglas (Fig. 3.4). A 3D simulation was implemented in k-Wave to simulate linear ultrasonic wave propagation. Nonlinearity in the media was ignored to simplify the analysis.

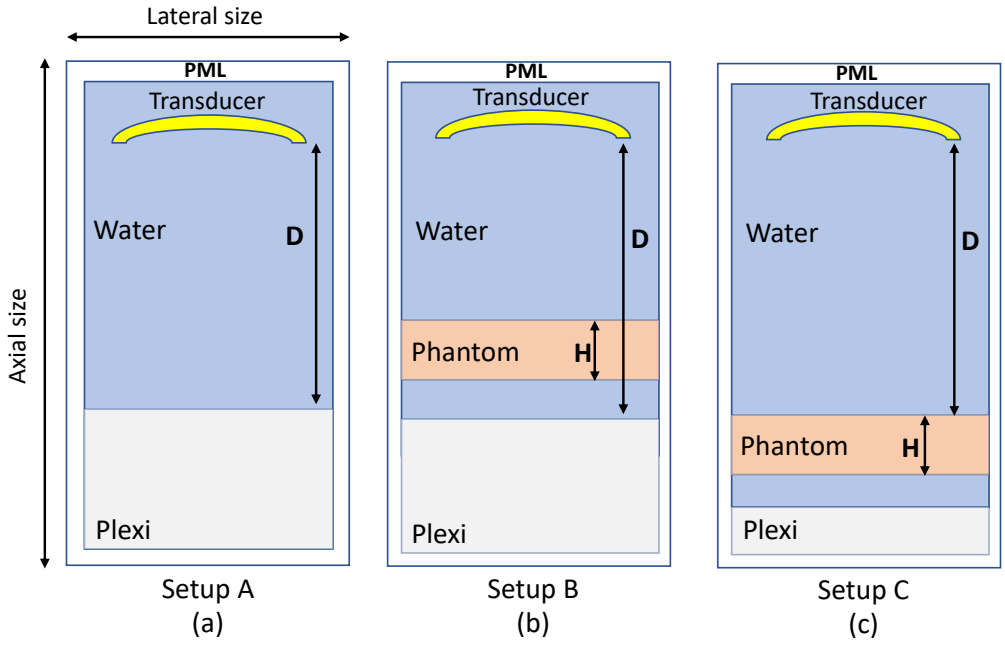

Fig. 3.4. Setups 1, 2, and 3 in k-Wave for simulating the proposed AC measurement technique (axial cross-section) replicate setups 1, 2, and 3 (in Fig. 3.2), respectively. The transducer position and domain size remained the same for the three setups. The planar focus, at a distance D from the transducer, was determined by maximizing the amplitude of the reference echo.

The grid spacing was chosen as low as possible based on available computational resources while satisfying the Nyquist criterion. k-Wave requires the attenuation exponent to be homogenous across the computational domain [19], whereas the attenuation exponent is different between phantom and water in practice. To address this issue, the same attenuation exponent of the phantom material was assigned to the entire domain. Consequently, a best-fit analysis was performed on the desired attenuation coefficients of water (Eq. (3.8)) and membrane over 2-30 MHz frequency range to match the attenuation exponent of the phantom. The transducer was simulated by defining points in the 3D medium along the contour of the spherically focused transducer. The transmit and receive electromechanical responses were each defined as Gaussian with a fractional bandwidth (-3 dB) of 50%.

3.3.2. Test Conditions

Simulations were performed to validate the proposed technique for two phantom-transducer combinations. The acoustic properties of all the materials (Table 3.1) were kept constant for both simulations. The transducer and phantom properties (Table 3.2) were chosen to represent typical use scenarios. Accordingly, the properties of the computational domain were chosen to make the simulation computationally tractable while ensuring reasonable accuracy as discussed in the following subsection. Finally, the methodological steps enumerated in section 3.2.3 were applied in k-Wave for both simulations.

Table 3.1. Material acoustic properties in simulation

Property	Phantom material	Membrane	Plexiglas	Water
Density (kg/m^3)	1040	1690	1180	1000
Sound speed (m/s)	1540	2400	2758	1480
Attenuation (dB/cm)	$0.400\ f^{1.3}$	$0.788\ f^{1.3}$	0	$0.016\ f^{1.3}$

3.2. Transducer, phantom, and domain properties across simulations

Property		Simulation 1	Simulation 2
Transducer	Center frequency (MHz)	10	20
	Diameter (mm)	9.0	6.4
	F#	4	4
Phantom	Phantom thickness (mm)	25.0	12.0
	Membrane thickness (μm)	63.9	64.0
Computational domain	Spatial resolution (μm)	21.3	16.0
	Time step (ns)	1.93	1.45

3.3.3. Quantifying the accuracy of k-Wave simulations

For a given grid spacing, the accuracy of k-Wave simulations with heterogeneous media reduces with an increase in ultrasonic frequency [24]. To quantify this effect, additional simulations were run while keeping the grid spacing constant. In these simulations, a broadband plane wave was normally incident onto the Plexiglas and membrane surfaces. The corresponding frequency-dependent pressure reflection and transmission coefficients were computed by recording the resulting ultrasonic waves. The simulated coefficients were compared with their true values, as programmed in the simulation, to yield an error estimate. Frequency-dependent simulated error estimates of $|R_1(f)|$ and $|T_{roundtrip}(f)|$ are expressed in points per wavelength (PPW) (Fig. 3.5(a) and 3.5(b), respectively).

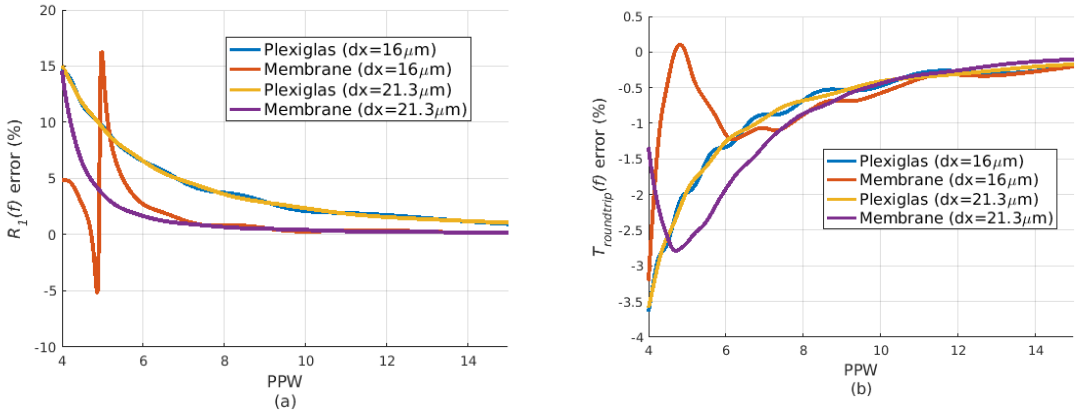

Fig. 3.5. Error in modeling water-Plexiglas and water-membrane-phantom surfaces for grid spacings of 16.0 µm and 21.3 µm across frequency (expressed in PPW). (a) Pressure reflection coefficient error, and (b) pressure transmission coefficient error.

Based on the memory available for the simulation, a reasonable error threshold of +10% on the reflection coefficient and –3% on the transmission coefficient were adopted for both surfaces leading to a frequency threshold of 5 PPW. This frequency threshold corresponds to an upper threshold of 18.5 MHz for a spatial resolution of 16.0 µm (used with the 20 MHz transducer) and 13.9 MHz for 21.3 µm (used with the 10 MHz transducer). Moreover, the inaccuracies arising from the discretization of the 64 µm membrane with a spatial resolution of 16.0 µm or 21.3 µm are also accounted for in this test.

3.3.4. Performance metrics

The accuracy of each simulation was quantified as

$$\Delta_{AC}(f) = \mu_{AC,P}(f) - \mu_{AC,R}(f), \tag{3.12}$$

where $\mu_{AC,P}$ is the acquired AC value and $\mu_{AC,R}$ is the pre-defined phantom AC profile in the code. Furthermore, root-mean-square values were computed for $\Delta_{AC}(f)$ for both simulations in their respective bandwidths.

3.4. Experimental validation

AC measurements were performed using conventional methods and methods proposed herein on five phantoms with diverse attenuation profiles. The AC results from both methods were compared to validate the proposed method. Furthermore, multiple individual measurements were performed by two different operators to assess the repeatability and cross-operator reproducibility of the measurements [41].

3.4.1. Setup

Single-element transducers in a pulse-echo configuration were used for measuring the phantom AC. Plexiglas was used as the planar reference surface. The transducer, phantom, and Plexiglas were immersed in degassed water (Fig. 3.1). The transducer was connected to a pulser-receiver (UT340, UTEX Scientific Instruments Inc., Mississauga, ON, Canada) followed by a digitizer (PDA14-200 A/D converter, Signatec Inc, Lockport, IL), with a sampling frequency of 200 MHz, to digitize the received analog echoes.

3.4.2. Test conditions

AC measurements were performed on five phantoms, named Phantom 1 to Phantom 5 (CIRS, Inc., Norfolk, VA, USA). The phantoms were made of different tissue-mimicking materials but were laminated with the same 25 μm-thick Saran membrane with well-studied properties [25]. While the conventional method incorporated this prior knowledge of the Saran membrane in the AC measurement, the proposed technique estimated the membrane properties for each phantom-transducer combination. Five weakly focused transducers (Table 3.3), spanning a frequency range of 0.7-16 MHz, were used in the validation. Two operators performed three AC measurements each for all the transducer-phantom combinations. When characterizing with the 12.7 MHz transducer (Transducer 5), the attenuation echoes (E_3) from Phantom 1 and Phantom 5 were below the receiver noise floor due to the two phantoms' high attenuation above 10 MHz. Hence, these two transducer-phantom combinations were dropped from the experiment. For each of the remaining transducer-phantom combinations, the intersection of the -20-dB bandwidths of the reference echo and the attenuation echo was chosen as the bandwidth for AC analysis.

Table 3.3. Properties of transducers used in the phantom AC measurements

Transducer ID	Part number	Center frequency (MHz)	Diameter (mm)	F#	Planar focus (D) (mm)
1	IL1506HR (Valpey Fisher Inc., Hopkinton, MA)	1.6	19.1	4	72.4
2	V382 (Panametrics Inc., Waltham, MA)	3.8	12.7	4	73.8
3	IL0506HR (Valpey Fisher Inc., Hopkinton, MA)	5.4	19.1	3	56.9
4	V321 (Panametrics Inc., Waltham, MA)	8.1	19.1	4	75.0
5	IS1004HR (Valpey Fisher Inc., Hopkinton, MA)	12.7	12.7	4	54.4

3.4.3. Performance metrics for the proposed method

The conventional method was used as a reference to quantify the accuracy of the proposed method. Consequently, Δ_{AC} was calculated for each transducer-phantom combination using Eq. (3.12) where $\mu_{AC,P}$ and $\mu_{AC,R}$ were AC averaged across iterations and operators for the proposed and reference methods, respectively. Repeatability and cross-operator reproducibility were quantified by calculating the sample standard deviation ($s_{AC}(f)$) across six measurements (three iterations x two operators) for each transducer-phantom combination. Furthermore, root-mean-square (RMS) $\Delta_{AC}(f)$ and $s_{AC}(f)$ were calculated for each phantom, for all transducers. Also, $s_{AC}(f)$ was normalized by $\mu_{AC,P}$ to calculate the coefficient of variation as

$$cov_{AC}(f) = \frac{s_{AC}(f)}{\mu_{AC,P}(f)} \tag{3.13}$$

3.5. Results

The results of a simulation-based and an experimental implementation of the proposed phantom AC measurement method are detailed in this section.

3.5.1. Simulation results

The acquired AC and corresponding accuracy metric, Δ_{AC}, are shown for both simulations in Fig. 3.6(a) and 3.6(b), respectively. The acquired $|R_1(f)|$ and the estimated $|T_{roundtrip}(f)|$ are shown for both simulations in Fig. 3.7(a) and 3.7(b), respectively. The RMS Δ_{AC} were 0.029 dB/cm-MHz and 0.049 dB/cm-MHz for the 25 mm and 12 mm phantoms, respectively. $|T_{roundtrip}(f)|$ varied between 0 to -14.5 dB within a frequency range of 3.5-18.5 MHz and was estimated within 0 to 2 dB error. The maximum error occurred at the peaks and nulls of the membrane transmission coefficient.

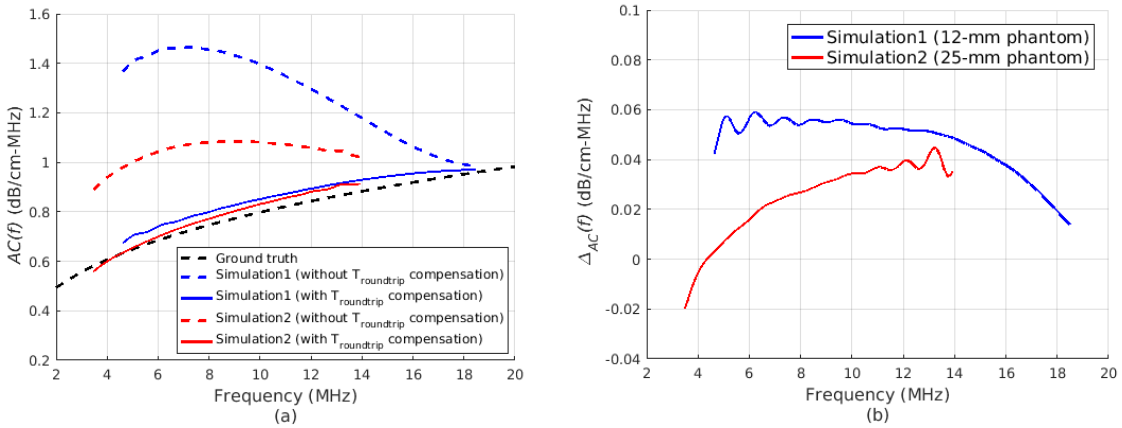

Fig. 3.6. (a) Acquired AC (with and without membrane $T_{roundtrip}$ compensation) compared with ground truth for simulations 1 and 2. (b) Difference between acquired AC and the ground truth for simulations 1 and 2.

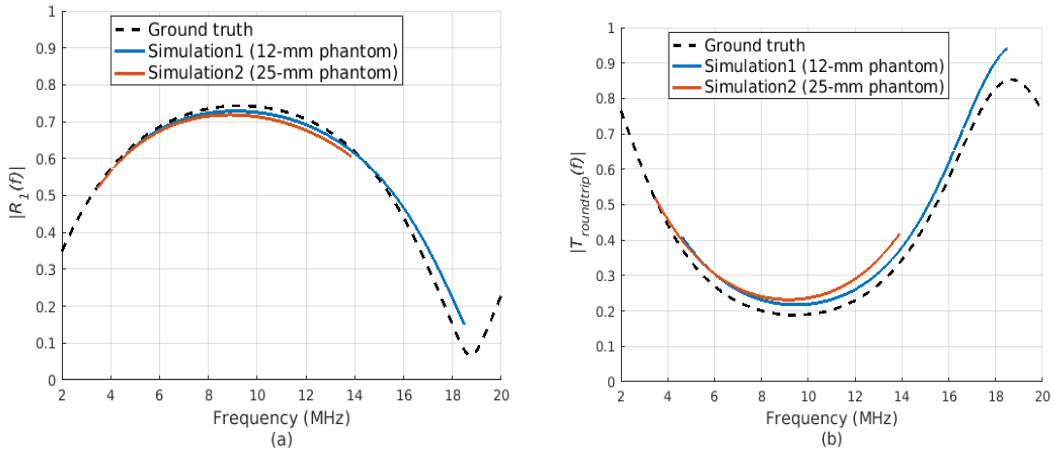

Fig. 3.7. (a) Membrane reflection coefficient (magnitude), acquired from both simulations, compared with ground truth. (b) Estimated membrane round-trip transmission coefficient (magnitude) compared with ground truth.

3.5.2. Experimental results

The measured AC, measured $|R_1(f)|$, and estimated $|T_{roundtrip}(f)|$ for all the phantom-transducer combinations, averaged across operators and individual iterations, are shown in Figs. 3.8, 9(a) and 9(b), respectively. The performance metrics for the proposed method, $\Delta_{AC}(f)$ and $s_{AC}(f)$, are shown in Figs. 3.10(a) and 3.10(b), respectively. Finally, for each phantom, Table 3.4 listed the RMS $\Delta_{AC}(f)$, the RMS $s_{AC}(f)$, and the mean coefficient of variation, and compared with their respective ACs.

Across all the five phantoms, RMS Δ_{AC} was 0.025 dB/cm-MHz and RMS s_{AC} was 0.018 dB/cm-MHz. $|T_{roundtrip}(f)|$ varied between 0 to -–11.8 dB within a frequency range of 0.7-16 MHz and was estimated within 0 to 3.5 dB error. The maximum error occurred at the null of the membrane transmission coefficient.

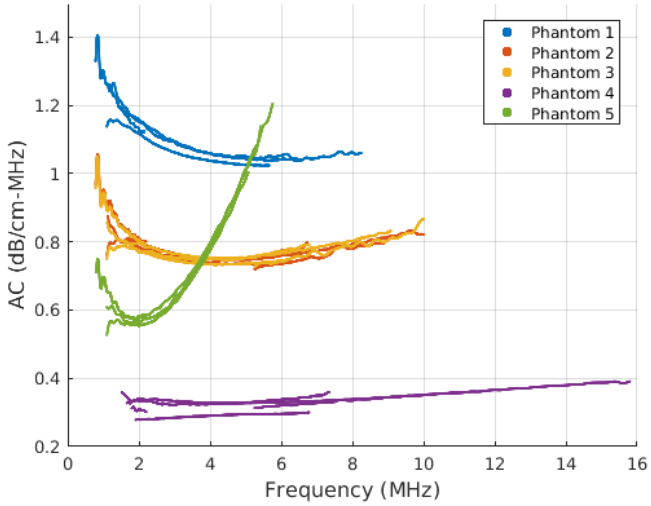

Fig. 3.8. Measured AC across phantoms and transducers (averaged across operators and individual iterations). For each phantom, multiple curves are present in each frequency range due to measurements from multiple transducers with overlapping bandwidths.

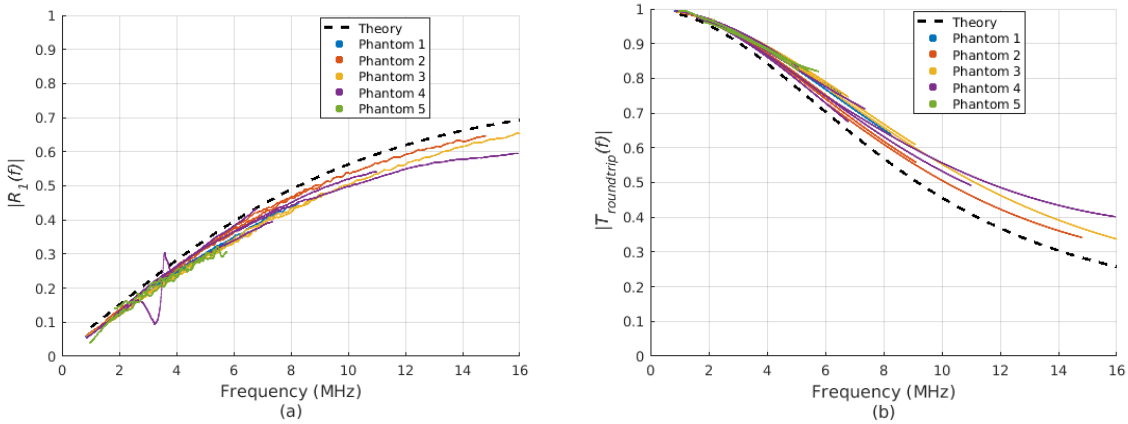

Fig. 3.9. Membrane characterization results averaged across operators and individual iterations and compared with the theoretical value [20]. (a) Measured membrane reflection coefficient (magnitude). (b) Estimated membrane round-trip transmission coefficient (magnitude).

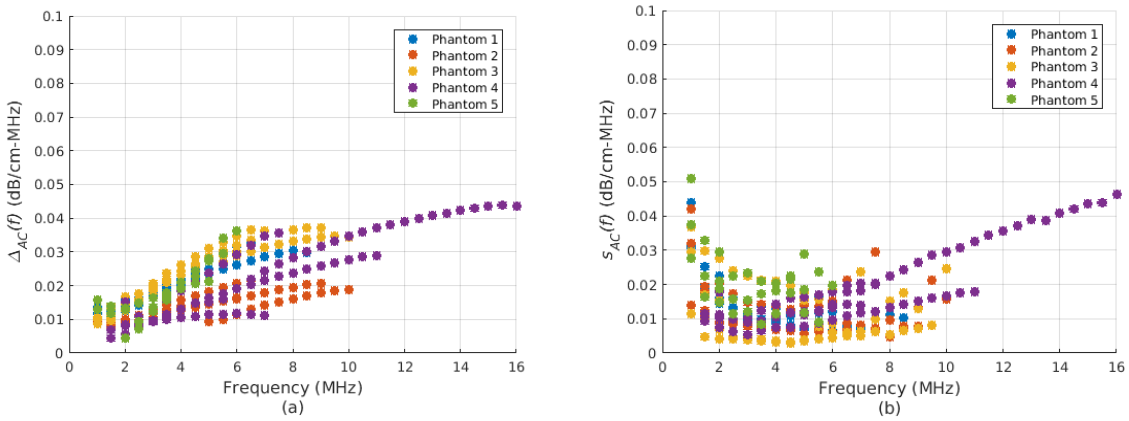

Fig. 3.10. Performance metrics calculated for the proposed method. AC is averaged within a bandwidth of 0.5 MHz, computed across operators and individual iterations (a) AC difference compared to the conventional method. (b) Sample standard deviation of the AC results.

Table 3.4. Performance metrics of the proposed method across phantoms

Phantom	$AC(f)$ Range (dB/cm-MHz)	RMS Δ_{AC} (dB/cm-MHz)	RMS s_{AC} (dB/cm-MHz)	Mean cov_{AC}
1	1.021 – 1.475	0.022	0.016	0.013
2	0.728 – 1.011	0.015	0.014	0.015
3	0.734 – 0.976	0.027	0.014	0.015
4	0.281 – 0.388	0.032	0.021	0.054
5	0.557 – 1.160	0.022	0.023	0.030

3.6. Discussion

This section discusses the conclusions that can be drawn from the simulation-based and the experimental validation of the proposed AC measurement method. It also details possible improvements to the method that can be pursued in the future.

3.6.1. Validation in k-Wave

The proposed method was successfully evaluated by k-Wave simulations by implementing two hypothetical transducer-phantom combinations. In Simulation 1, a 12 mm phantom's AC ranging from 0.5-0.9 dB/cm-MHz over 4.6-18.5 MHz was successfully measured with a maximum

error of 0.060 dB/cm-MHz. In Simulation 2, a 25 mm phantom's AC ranging from 0.6-1.0 dB/cm-MHz over 3.5-13.9 MHz range was successfully measured with a maximum error of 0.045 dB/cm-MHz. AC acquired without membrane transmission loss compensation was plotted (Fig. 3.6(a)) for both simulations to illustrate the importance of accounting for membrane effects in the AC measurement. Without membrane loss compensation, Simulations 1 and 2 had a maximum Δ_{AC} of 0.76 and 0.36 dB/cm-MHz, respectively, which is significant compared to ground truth AC in the same bandwidth. Also, the phantom insertion could have changed the diffraction pattern between Setup 1 and Setup 2 of Fig. 3.2, potentially introducing diffraction artifacts while calculating the insertion loss. However, this change was found to be negligible in simulations by an analysis of the beam patterns with and without phantom insertion. This is expected since the sound speed of the reference phantom material is close to that of water.

3.6.2. Experimental validation

The proposed method successfully measured phantom ACs with diverse attenuation profiles. The laboratory experiments compared the proposed AC measurement technique with the conventional technique and evaluated its accuracy across transducers and phantom attenuation profiles. While the phantoms' AC varied between 0.28 to 1.48 dB/cm-MHz over 0.7-16 MHz, the proposed AC method had a maximum error of only 0.045 dB/cm-MHz (see Fig. 3.10(a)) relative to the conventional method. For a given phantom, there was continuity in the measured $AC(f)$ for two transducers with overlapping bandwidths. Also, the method was accurate for weakly focused transducers, typically used in QUS applications, with F# between 3 and 4. Finally, the proposed method showed good repeatability and cross-operator reproducibility, with a mean coefficient for variation between 0.013 and 0.054.

3.6.3. Possible improvements to the membrane estimation algorithm

The membrane transmission coefficient's accuracy was estimated in simulation and experimentally (Fig. 3.7(b) and 3.9(b), respectively). The error in the estimated $|T_{roundtrip}(f)|$ emerged from the acquired $|R_1(f)|$ that showed a discrepancy in the amplitude and position of nulls and peaks. This discrepancy is possibly due to the nonplanar wavefronts at the focus of transducers used in this study, thus violating the planar wave assumption. Diffraction correction can be applied to compensate for the error in estimated $|T_{roundtrip}(f)|$. Currently, the main source

of error in determining AC is the membrane estimation step. For instance, an error of 2 dB in estimated $20\log_{10}|T_{roundtrip}|$ at 10 MHz would lead to a Δ_{AC} of 0.04 dB/cm-MHz for a 25 mm phantom (Eq. (3.11)). These values closely match the observed error in estimated $|T_{roundtrip}|$ and Δ_{AC} for Simulation 1 at 10 MHz (Fig. 3.6(b) and 3.7(b), respectively). For the same reason, Δ_{AC} for the thinner phantoms (e.g., 12 mm phantom) is greater than the Δ_{AC} of the thicker phantoms (e.g., 25 mm phantom). Hence, the improvement in membrane estimation will further improve the AC measurement technique. Since an analytical model for diffraction correction will be complicated, a simulation study in k-Wave can be useful instead and perhaps can even lead to an empirical correction factor. Alternatively, as the phantom thickness increases, the accuracy increases for the proposed AC measurement technique.

The membrane is assumed to be nonattenuative in the estimation procedure. This assumption is reasonable in typical scenarios since the cumulative attenuation offered by a thin membrane, $AC_M(f)fL$, is much less than $20\log_{10}|T_{roundtrip}(f)|$. However, this assumption can fail if the membrane is thick, or highly attenuative, or both. In such cases, membrane attenuation can be incorporated in the reflection and transmission coefficients by representing the membrane wavenumber (k_2) as a complex number

$$k_2 = \frac{2\pi f}{c_2} - j\alpha_{\mathrm{M}}(f), \tag{3.14}$$

where $\alpha_M(f)$ is the frequency-dependent attenuation coefficient (in Np/m) of the membrane [25]. Then, the estimation procedure would also estimate $\alpha_{\mathrm{M}}(f)$ along with Z_2, Z_3, and L/c_2.

CHAPTER 4
SIMULATING AND VALIDATING ACOUSTIC BACKSCATTER FOR A SINGLE SCATTERER IN K-WAVE

4.1 Motivation to simulate backscatter in k-Wave

Acoustic backscatter is quantified by the backscatter coefficient (BSC). For a given tissue, BSC is a fundamental property independent of operator and equipment and has been shown to enhance contrast in ultrasonic imaging of the eye [33], prostate [32], kidney [31], blood [42] [43], breast [44]–[46], and liver [29]. Crucially, BSC is directly related to the acoustic properties of the tissue microstructure. So, numerous studies have attempted to build a forward model linking tissue histology to the observed BSC [47]–[49]. The inverse problem was then solved to obtain quantitative estimates of tissue properties such as scatterer size and scatterer concentration.

Mamou et al. built acoustic 3D impedance maps (3DZM) of soft tissues from histology. The BSC was analytically computed by applying spatial FFT to the 3D impedance map. The computed BSC was then used to choose appropriate scattering models to fit the observed BSC. This method yielded more accurate estimates of acoustic scatterer size and consequently in better classification of mammary tumors. However, Mamou et al. made some assumptions in their work that can be improved upon due to recent advances in acoustic simulation software and computing power. First, the incident acoustic waves are assumed to be planar, and the scattered acoustic waves are assumed to be spherical in the far-field. Second, they assumed weak scattering or weak medium heterogeneity wherein the impedance contrast between the background and the scatterer was low (less than 10%). Third, multiple scattering was assumed to be absent. Finally, the transducer was not simulated, and the medium attenuation was ignored.

Kemmerer [7] implemented the 3DZM in Field-II acoustic simulation software to include the transducer in the backscatter modeling while retaining the rest of the assumptions from Mamou et al. Specifically, the assumption of weak scattering in soft tissues can be a limitation for impedance contrasts higher than 7% as shown in Fig. 4.1. In this figure, the exact BSC of a

spherical scatterer from Anderson's theory [50] is normalized and plotted. While the normalized-BSC is similar in shape for low impedance contrasts, there is a marked change for the higher impedance contrasts. Hence the spatial FFT approach for calculating BSC is inaccurate for impedance contrasts higher than 7%. Such contrasts are realistic in many clinical ultrasound applications as highlighted in Table 4.1. Furthermore, even the tumor 3DZMs used by Mamou et al. had impedance contrasts up to 16%, as shown in Table 4.2.

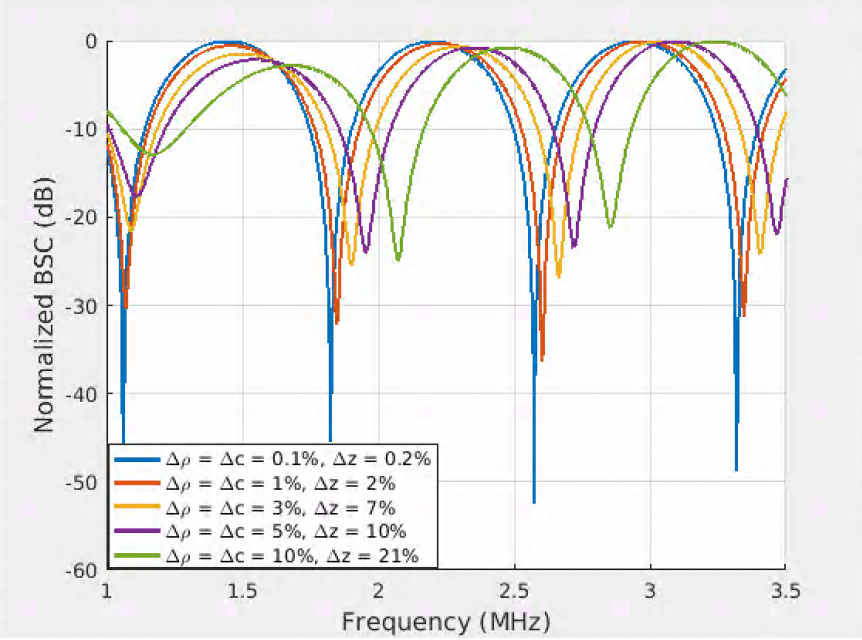

Fig. 4.1. Theoretical Anderson BSC (normalized by the peak value within the bandwidth) of a spherical scatterer (1 mm diameter) across impedance contrast.

Table 4.1. Acoustic impedance values of selected media [51]
(Reference impedance (Z_0) = 1.54 MRayl)

Medium	Z (MRayl)	$\Delta Z/Z_0$ (%)
Water (20° C)	1.48	-3.90
Fat	1.38	-10.39
Kidney	1.65	7.14
Skin	1.99	29.22
Brain	1.60	3.90
Muscle	1.71	11.04
Blood	1.66	7.79
Liver, Muscle	1.69	9.74
Eye (lens)	1.72	11.69
Eye (vitreous humor)	1.54	0.00

Table 4.2. Acoustic impedance values used for the 3DZMs by Mamou et al. [48]

Tumor	Medium	Z (MRayl)	$\Delta Z/Z_0$ (%)
Rat fibroadenoma	Connective tissue (Z_0)	1.80	0.00
	Epithelial cells	1.58	-12.22
	Mammary duct	1.54	-14.44
4T1 mouse mammary carcinoma	Background (Z_0)	1.55	0.00
	Connective tissue	1.80	16.13
	Cytoplasm	1.58	1.94
	Nuclei	1.60	3.23
	Red blood cells	1.60	3.23

Furthermore, the region of interest often lies beneath other strongly heterogeneous tissue layers such as skin, fat, and muscle which might violate assumptions of plane wave incidence and necessitate the incorporation of acoustic reflection and transmission in BSC extraction methods. K-Wave is well suited to address these gaps in 3DZM modeling since it implements full-wave simulation [52] for heterogeneous and nonlinear media while supporting acoustic reflection, transmission, and scattering. By modeling the full range of acoustic phenomena, such a model can also aid in the design of better transducers and excitation schemes for tissue BSC extraction. In

addition, k-Wave supports shear waves in solid media. Therefore, the 3DZM-BSC modeling can potentially be extended to calcaneal quantitative ultrasound, harmonic imaging, and transcranial applications. The 3DZM-BSC model can also be useful in training neural networks that have been shown to improve specificity in QUS applications [53]. In such contexts, the backscatter generated from synthetic or histological 3DZM models can be used as training data. Since the ground truth BSC is known, the neural network can be made more accurate, interpretable, and robust.

There have been a few simulation studies in k-Wave examining acoustic scattering. Parker et al. [8] simulated acoustic backscatter from randomly placed cylinders in a 3D medium to examine the dependence of B-mode speckle on number density. Song et al. [9] simulated acoustic through-transmission for a collection of spherical scatterers in a 3D medium to examine the effect of multiple scattering on fine dust number density estimation. Santos [10] simulated acoustic through-transmission for a spherical scatterer collection in a 3D medium to examine the dependence of iron nodule number density on ultrasonic scattering attenuation. However, no simulation study in k-Wave has addressed the acoustic backscatter and extraction of spectral BSC. The work presented in Chapters 4-6 fills this gap and extends it to basic 3DZMs. As a first step in simulating 3DZMs in k-Wave, backscatter from a single spherical scatterer will be examined in this chapter.

4.2 Acoustic scattering theory for single scatterers

When acoustic plane waves are incident on a medium, the scattered waves in the far-field are spherical as shown in Fig. 4.2.

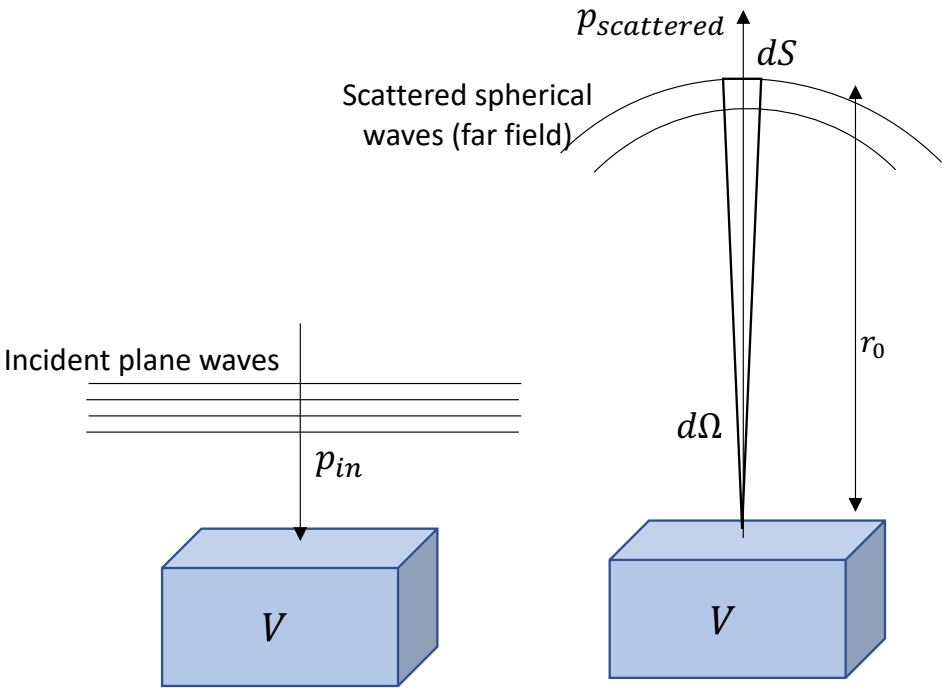

Fig. 4.2. Quantifying acoustic scattering from a medium.

Then, the differential backscattering cross-section as a function of frequency f is defined as [54]

$$\sigma_b(f) = \frac{d}{d\Omega}\left(\frac{time-averaged\ backscattered\ power}{time-averaged\ incident\ intensity}\right)$$

$$= \frac{|p_{scattered}(f,r_0,\theta=\pi)|^2\, dS}{|p_{in}(f)|^2 \cdot d\Omega} = \frac{|p_{scattered}(f,r_0,\theta=\pi)|^2\, r_0^2}{|p_{in}(f)|^2}, \qquad (4.1)$$

where r_0 is the distance between scattering volume V and observational area dS, $d\Omega$ is the differential angle subtended by dS, p_{in} is the pressure amplitude of the incident acoustic plane wave, and $p_{scattered}$ is the pressure amplitude of the scattered acoustic wave.

Similarly, the backscatter coefficient (BSC) as a function of frequency f is defined as [54]

$$\sigma_{bsc}(f) = \frac{\sigma_b(f)}{V}$$

$$= \frac{|p_{scattered}(f,r_0,\theta=\pi)|^2\, dS}{|p_{in}(f)|^2 \cdot d\Omega \cdot \mathrm{V}} = \frac{|p_{scattered}(f,r_0,\theta=\pi)|^2\, r_0^2}{|p_{in}(f)|^2 \cdot \mathrm{V}} \quad . \qquad (4.2)$$

Analytical expressions for the differential backscattering cross-section can be derived from literature for simple shapes such as spheres [50], [55], cylinders [56], and concentric spheres [57]. This work will focus on 3DZMs constituted with fluid spheres. Consequently, the Anderson model was used in analyzing the differential backscattering cross-section which is given as

$$\sigma'_{b,Anderson}(f, r_0) = \left|\sum_{m=0}^{\infty}\left[\frac{(-i)^m(2m+1)}{(1+iC_m)}\right][j_m(kr_0) + in_m(kr_0)]\right|^2 r_0^2 \,, \qquad (4.3)$$

$$C_m = \frac{\left[\left[\frac{\alpha_m(k'a)}{\alpha_m(ka)}\right]\left[\frac{n_m(ka)}{j_m(k'a)}\right] - \left[\frac{\beta_m(ka)}{\alpha_m(ka)}\right]\left[\frac{\rho' c'}{\rho\, c}\right]\right]}{\left[\left[\frac{\alpha_m(k'a)}{\alpha_m(ka)}\right]\left[\frac{j_m(ka)}{j_m(k'a)}\right] - \left[\frac{\rho' c'}{\rho\, c}\right]\right]}, \qquad (4.4)$$

$$\alpha_m(kr) = mj_{m-1}(kr) - (m+1)j_{m+1}(kr) \,, \qquad (4.5)$$

$$\beta_m(kr) = mn_{m-1}(kr) - (m+1)n_{m+1}(kr) \,, \qquad (4.6)$$

where ρ, c are respectively background density and sound speed, and ρ', c' are respectively scatterer density and sound speed. Variables k and k' are respectively, background-wavenumber and scatterer-wavenumber ($k = 2\pi f/c$ and $k' = 2\pi f/c'$), and j_m and n_m are spherical Bessel function of the first kind and spherical Bessel function of the second kind, respectively. For observation points in the far-field ($kr_0 \gg 1$), Eq. (4.3) reduces to

$$\sigma_{b,Anderson}(f) = \frac{c^2}{4\pi^2 f^2}\left|\sum_{m=0}^{\infty}\left[\frac{(-i)^m(2m+1)}{1+iC_m}\right]\right|^2 . \qquad (4.7)$$

In the subsequent sections, a single spherical scatterer will be acoustically examined by different transducers, and the differential backscatter cross-section will be extracted and compared with Anderson's theory. The goal was to design, validate and compare different schemes for backscatter parameter extraction that can be eventually extended to 3DZMs.

4.3 Methodology

Three schemes were examined for backscatter parameter extraction of a single spherical scatterer.

4.3.1 Single element focused transducer (*focused transducer scheme*)

In this scheme, the planar reference method of BSC extraction [1] was applied on a single spherical scatterer. A single element focused transducer was used as a pulse-echo transmitter-receiver, and Plexiglas was used as the planar reference as shown in Fig. 4.3. In Setup 1, Plexiglas was placed along the focal plane that gave the reference pressure echo p_r. In Setup 2, the scatterer's geometric center overlapped with the focal point of the transducer that gave the scattered pressure echo p_s. The received echoes in both cases were obtained by summation of the pressure signals received by the grid points on the transducer surface.

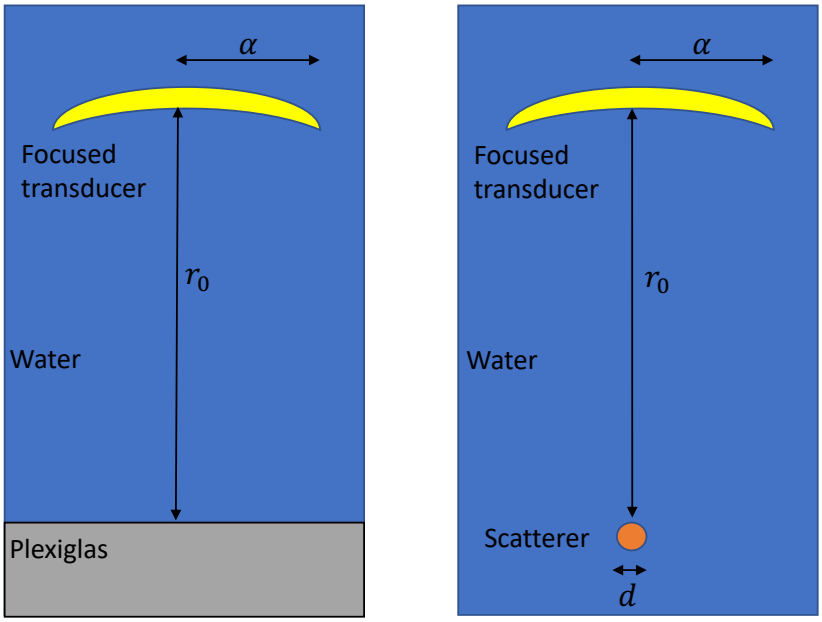

Fig. 4.3. Setups for the planar reference method of backscatter parameter extraction for a single scatterer. r_0 is the radius of curvature of the focused transducer, α is the radius of the aperture, and d is the scatterer diameter.

Implementation of this scheme in k-Wave was inspired by Kemmerer et al.'s work [7] where the scheme was implemented in Field-II. Therefore, this work followed Kemmerer et al. in choosing the scatterer size and the transducer dimensions which in turn was chosen to mirror experimental conditions. In particular, the single scatterer had a diameter that was comparable to the transducer beamwidth (51% to 177% of the beamwidth).

Next, the Chen method [1] of BSC extraction was modified for the single scatterer case. When applied to a random medium, the Chen equation to extract BSC for a planar reference method, assuming a unity receiver electro-mechanical transfer function, is given by (Eq. (31), [1])

$$\sigma_{bsc,random}(f) = \frac{<|p_s(r,f)|^2>}{|p_r(r_0,f)|^2} \cdot \frac{\gamma^2 \, |D_{ref}(r_0,f)|^2}{l \cdot <D_s(r,f)>}, \tag{4.8}$$

where $p_s(f)$ and $p_r(f)$ are the spectrum of the scattered pressure wave and the spectrum of reference pressure wave, respectively. Additionally, p_s is ensemble-averaged within the scattering region of interest (ROI) centered around the focus. Next, $< D_s(r,f) >$ is the mean diffraction correction function, l is the axial length of ROI, γ is the pressure reflection coefficient of the water-reference interface, and D_{ref} is the acoustic coupling function from the transducer surface to the reference plane and back to the transducer surface.

To apply Eq. (4.8) to the single scatterer, the scatterer can be assumed to be contained within an ROI cube of volume d^3. Hence, the ROI axial length l is equal to the scatterer diameter d. Next, the ensemble average of the scattered spectrum $< |p_s(r,f)|^2 >$ can be replaced with the scattered spectrum of the single scatterer at the focus $|p_s(r_0,f)|^2$. Finally, the mean diffraction correction, $< |D_s(r,f)| >$ must be averaged only within the ROI cube. This is calculated using Equations (2) and (20) of [1] which are given by, respectively,

$$D(r,f) = -\frac{ik}{2\pi} \iint_{S_R}^{S_R} \frac{\chi(\boldsymbol{r_t}) \exp(ik\,(\boldsymbol{r}-\boldsymbol{r_t}))}{\boldsymbol{r}-\boldsymbol{r_t}} \, dS(\boldsymbol{r_t}), \tag{4.9}$$

$$< |D_s(r,f)| >= \frac{1}{l} \cdot \left[\left(\frac{2\pi}{kS_R} \right)^2 \iiint |D(r,\omega)|^4 dV \right], \tag{4.10}$$

where χ is the relative sensitivity of each point on the transducer, which is set to one in the simulation, k is the background wavenumber ($k = 2\pi f/c$), and S_R is the active transducer area given by

$$S_R = 2\pi r_0^2\left(1 - \sqrt{1 - (\alpha/r_0)^2}\right). \tag{4.11}$$

Evaluating Eq. (4.9) at r_0, we get

$$D(r_0, f) = -\frac{ik}{2\pi} \cdot \frac{\exp(ikr_0)}{r_0} S_R \ . \tag{4.12}$$

The mean diffraction inside the ROI cube is reasonably assumed to be constant since the scatterer dimension is comparable to the beamwidth, and the axial length of ROI is d. Then, Eq. (4.10) reduces to

$$< |D_s(r,f)| > = \frac{1}{d}\left[\left(\frac{2\pi}{kS_R}\right)^2 |D(r_0,f)|^4 d^3\right] = k^2\left(1 - \sqrt{1 - (\alpha/r_0)^2}\right)d^2 \ . \tag{4.13}$$

Next, the acoustic coupling function between the transducer and planar reference is given by Eq. (57) of [1]

$$|D_{ref}(r_0, \omega)| = \left|1 - \exp(-iG_p)\left\{J_0(G_p) - iJ_1(G_p)\right\}\right| \ , \tag{4.14}$$

where J_0 and J_1 are Bessel functions of zeroth and first kind, respectively. G_p is the pressure gain factor given by

$$G_p = \frac{k\alpha^2}{2r_0} . \tag{4.15}$$

Finally, by combining Equations (4.8), (4.13) – (4.15), the single scatterer BSC is extracted as

$$\sigma_{bsc,single}(f) = \frac{|V_s(r_0,f)|^2}{|V_r(r_0,f)|^2} \cdot \frac{\gamma^2 \left|1-\exp(-iG_p)\{J_0(G_p)-i\,J_1(G_p)\}\right|^2}{k^2\left(1-\sqrt{1-(\alpha/r_0)^2}\right)\cdot d^3} . \tag{4.16}$$

Next, the differential backscatter cross-section for the single scatterer can be derived from Equations (4.2) and (4.16) as

$$\sigma_{b,single}(f) = \frac{|V_s(r_0,f)|^2}{|V_r(r_0,f)|^2} \cdot \frac{\gamma^2 \left|1-\exp(-iG_p)\{J_0(G_p)-iJ_1(G_p)\}\right|^2}{k^2\left(1-\sqrt{1-(\alpha/r_0)^2}\right)}. \tag{4.17}$$

4.3.2 Wide planar transmitter and point receiver (*near-field scheme*)

In this scheme, the simulation was set up to extract the exact differential backscatter cross-section of the single scatterer. This scheme was realized by recreating the ideal assumptions for computing backscatter parameters wherein the incident waves are planar, and the receiver is placed in the far-field (relative to the scatterer). By placing the scatterer in the near field of a wide planar transmitter, as shown in Fig. 4.4, the incident waves were ensured to be planar. Next, a point receiver was placed above the planar transmitter in the backscatter direction ($\theta = \pi$) to record the backscattered pressure wave.

Fig. 4.4. Setups for the *near-field scheme* of backscatter parameter extraction for a single scatterer. In the figure, w is the width of the planar transducer, r_t is the distance between transmitter and scatterer, r_r is the distance between scatterer and receiver, and d is the scatterer diameter.

Then, the differential backscatter cross-section for the single scatterer can be obtained from Eq. (4.1) as

$$\sigma_b(f) = \frac{|p_s(f)|^2\, r_r^2}{|p_r(f)|^2}, \tag{4.18}$$

where $p_r(f)$ is the spectrum of the incident pressure pulse obtained from Setup 1 and $p_s(f)$ is the spectrum of the backscattered pressure pulse obtained from Setup 2.

The envelope of the pressure wave across different time points for a configuration of Setup 2 are plotted in Fig. 4.5 which will help visualize the wavefronts, and in choosing the setup parameters (w, r_t, and r_r).

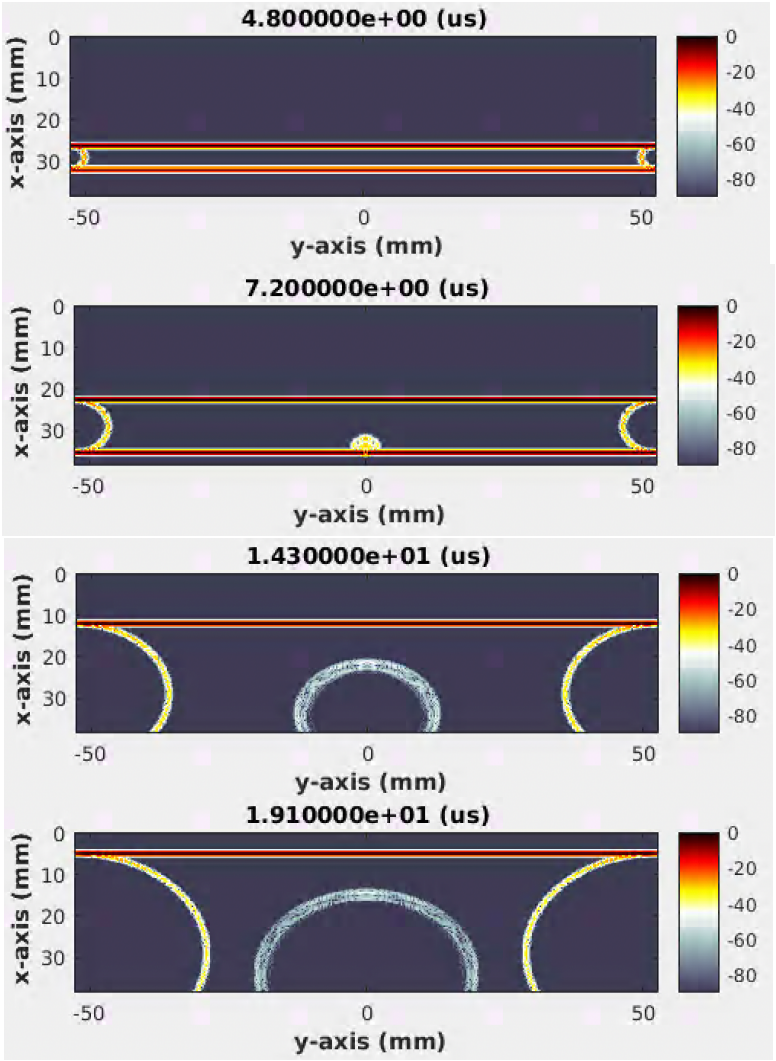

Fig. 4.5. Envelope of the pressure field (normalized by the peak pressure across the entire simulation time) at four time points for a configuration of Setup 2 (w = 100 mm, d = 1 mm, r_t = 4 mm, and spatial pulse length (SPL) = 2 mm). Vertical cross-section of the 3D domain. (a) The wavefront is planar as it is incident on the scatterer. (b) Initial moments of wave incidence on the spherical scatterer. The planar transmitter's edges, at the domain boundary, produce cylindrical waves which are undesirable. Setup parameters must be appropriately chosen such that the cylindrical waves do not overlap with the incident pulse p_r, or the scattered pulse p_s used for backscatter processing. (c) and (d) Show further evolution of the scattered spherical wave and the undesirable edge-generated cylindrical wave.

From Fig. 4.5, the following constraints were chosen to exclude cylindrical waves from the incident pulse p_r or the scattered pulse p_s

$$r_t > SPL/2\ , \tag{4.19}$$

$$\sqrt{(r_r - r_t)^2 + (w/2)^2} > r_t + r_r + SPL\ . \tag{4.20}$$

In this work, a -80dB threshold was applied to the envelope of the excitation signal to obtain the spatial pulse length (SPL).

4.3.3 Piston transmitter and point receiver (*far-field scheme*)

A second scheme was designed to extract the exact differential backscatter cross-section of a single scatterer. In this scheme, the scatterer was placed along the axis in the far-field region of a piston transmitter as shown in Fig. 4.6. Consequently, the incident acoustic waves were approximately planar. Next, a point receiver was placed at the center of the piston transmitter to record the backscattered spherical waves. Thus, the receiver is ensured to be in the far-field region relative to the spherical scatterer. The piston transmitter was chosen for this scheme because of its well-studied beam pattern.

Given a scatterer diameter d and frequency bandwidth of interest, the setup parameters were appropriately chosen. Firstly, r_0 were larger than the Rayleigh distance so that the scatterer is in the far-field region of the transmitter which gives a constraint

$$r_0 > \pi\alpha^2 / \min\{\lambda\}\ , \tag{4.21}$$

where $\min\{\lambda\}$ is the minimum wavelength in the frequency bandwidth of interest. Next, the pressure variation inside the scatterer was constrained to be within ±10% (or ±1dB). To meet this constraint, the scatterer is located within the 1 dB beamwidth of the transverse plane which gives

$$d < (-1\ dB\ beamwidth) = \frac{\min\{\lambda\}\, r_0}{3\alpha}\ . \tag{4.22}$$

Now, the axial pressure in the far-field has a $1/r$ variation. So, r_0 is chosen such that

$$r_0 > 8d\ , \tag{4.23}$$

which ensures that the pressure variation in the axial direction is within ±5% inside the scatterer.

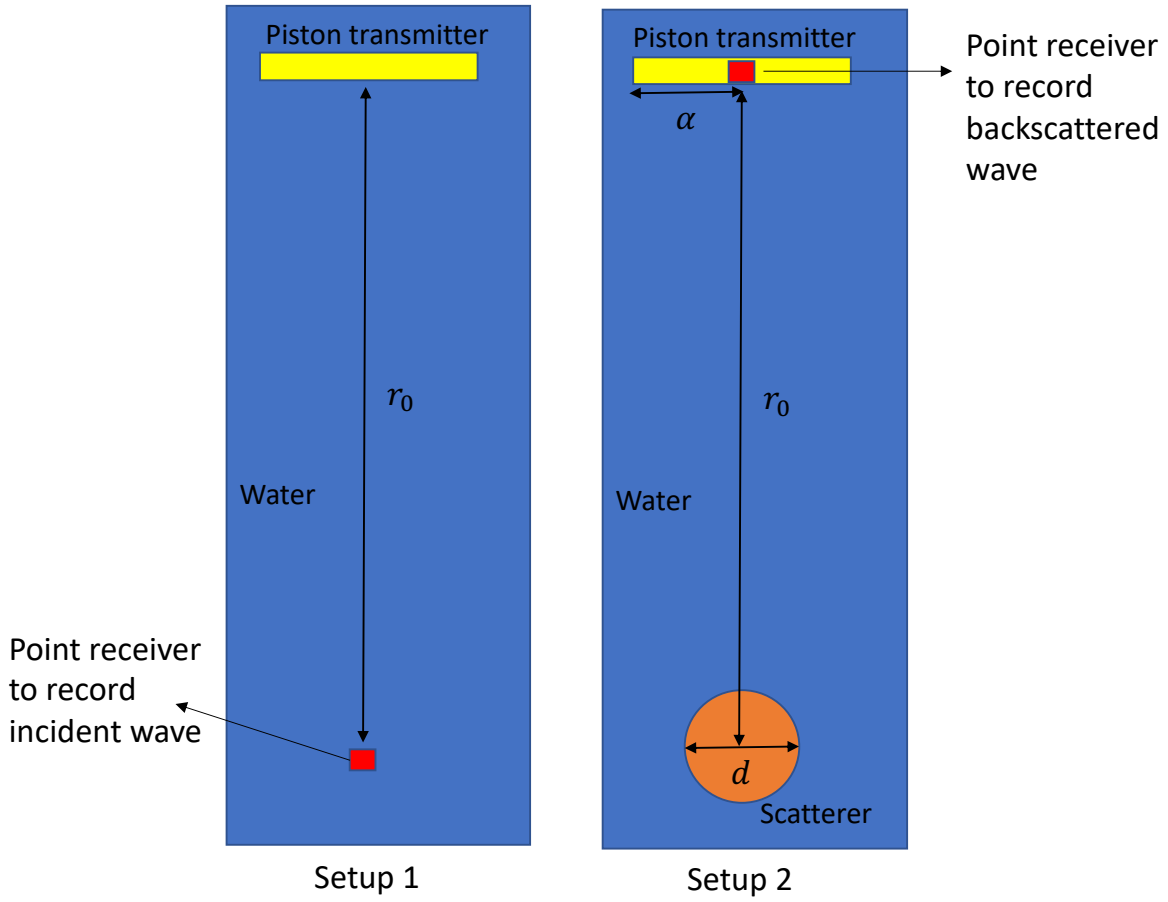

Fig. 4.6. Setups for the *far-field scheme* of BSC extraction for a single scatterer. In the figure, α is the radius of the piston transducer, r_0 is the distance between transmitter and scatterer, and d is the scatterer diameter.

4.3.4 Implementation and validation of backscatter parameter extraction schemes in k-Wave

We will examine a 1 mm scatterer in a frequency bandwidth of 1.5-3.5 MHz, following the parameters used by Kemmerer et al. to facilitate comparison. In all the simulations, the background is water with a sound speed of 1480 m/s and a density of 1000 kg/m^3. Two scatterers with different acoustic impedances were simulated: 1) *weak scatterer* (sound speed of 1495 m/s and density of 1010 kg/m^3) with an acoustic impedance 2% higher than the background and 2) *strong scatterer* (sound speed of 1628 m/s and density of 1100 kg/m^3) with an acoustic impedance 21% higher than

the background. As the names suggest, the *weak scatterer* showed weak impedance contrast whereas the *strong scatterer* showed strong impedance contrast.

The excitation signal for all the schemes was a 2.25 MHz sinusoid with a Gaussian envelope. As highlighted in Chapter 2, the accuracy of the simulation depends on the degree of spatial discretization. Where possible, the spatial resolution was varied between 12.5 μm to 52.6 μm to observe this effect. The time step was chosen such that CFL is 0.25. For the *focused transducer scheme*, 3D simulations could not be conducted due to large memory requirements. Instead, 2D axisymmetric simulations were conducted leveraging the cylindrical symmetry of setups around the axis. The simulation and setup parameters used to validate all the backscatter parameter extraction schemes are summarized in Tables 4.3 – 4.5.

For validation, the differential backscatter cross-section ($\sigma_b(f)$) was extracted for each of the schemes and compared with the reference Anderson theory ($\sigma_{b,reference}(f)$ from Eq. (4.3) or Eq. (4.7), as applicable). To quantify the accuracy, root mean square error (RMSE) was computed over the frequency bandwidth as

$$\sigma_{b,RMSE} = \sqrt{\frac{1}{N}\sum_{f_1}^{f_N} |\sigma_b(f) - \sigma_{b,reference}(f)|^2}\ . \tag{4.24}$$

Table 4.3. Setup parameters for the validation of *focused-transducer scheme* (2D axisymmetric simulation)

Parameters		Simulation 1	Simulation 2	Simulation 3
Transducer	Aperture (2α)	19.1 mm		
	The radius of curvature (r_0)	25.4 mm		
	Center frequency (f_0)	2.25 MHz		
	3-dB Bandwidth	50%		
Scatterer	Diameter (d)	1000.008 μm	999.999 μm	999.982 μm
	Sound speed	1495 m/s (*weak scatterer*) 1628 m/s (*strong scatterer*)		
	Density	1010 kg/m^3 (*weak scatterer*) 1100 kg/m^3 (*strong scatterer*)		
Background	Sound speed	1480 m/s		
	Density	1000 kg/m^3		
Reference (Plexiglas)	Sound speed	2758 m/s		
	Density	1180 kg/m^3		
Computational domain	Spatial resolution (dx)	52.632 μm	25.641 μm	12.658 μm
	Time step (dt)	4.771 ns	2.324 ns	1.147 ns

Table 4.4. Setup parameters for the validation of *near-field scheme* (3D simulation)

Parameters		Simulation 1	Simulation 2
Transducer	Width (w)	36 mm	25 mm
	Center frequency (f_0)	2.25 MHz	
	3-dB Bandwidth	30%	
Scatterer	Diameter (d)	1 mm	
	Sound speed	1495 m/s (*weak scatterer*) 1628 m/s (*strong scatterer*)	
	Density	1010 kg/m^3 (*weak scatterer*) 1100 kg/m^3 (*strong scatterer*)	
Background	Sound speed	1480 m/s	
	Density	1000 kg/m^3	
Other	Distance between transmitter and scatterer (r_t)	4 mm	
	Distance between receiver and scatterer (r_r)	3 mm	
Computational domain	Spatial resolution (dx)	50 μm	25 μm
	Time step (dt)	7.7 ns	3.8 ns

Table 4.5. Setup parameters for the validation of *far-field scheme* (3D simulation)

Parameters		Simulation 1	Simulation 2	Simulation3
Transducer	Radius of aperture (α)	500 µm		
	Center frequency (f_0)	2.25 MHz		
	3-dB Bandwidth	30%		
Scatterer	Diameter (d)	1 mm		
	Sound speed	1495 m/s (*weak scatterer*) 1628 m/s (*strong scatterer*)		
	Density	1010 kg/m^3 (*weak scatterer*) 1100 kg/m^3 (*strong scatterer*)		
Background	Sound speed	1480 m/s		
	Density	1000 kg/m^3		
Other	Transmitter-scatterer distance (r_0)	8 mm		
Computational domain	Spatial resolution (dx)	50 µm	25 µm	12.5 µm
	Time step (dt)	7.7 ns	3.8 ns	1.9 ns

4.4 Results

The differential backscatter cross-section (σ_b) extracted from *focused-transducer*, *near-field*, and *far-field* simulations are plotted in Figs. 4.7, 4.8, and 4.9, respectively. In these figures, the extracted differential backscatter cross-section results are compared with Anderson's theory. Additionally, root mean square error values were calculated for the differential backscatter cross-section results and tabulated in Table 4.6.

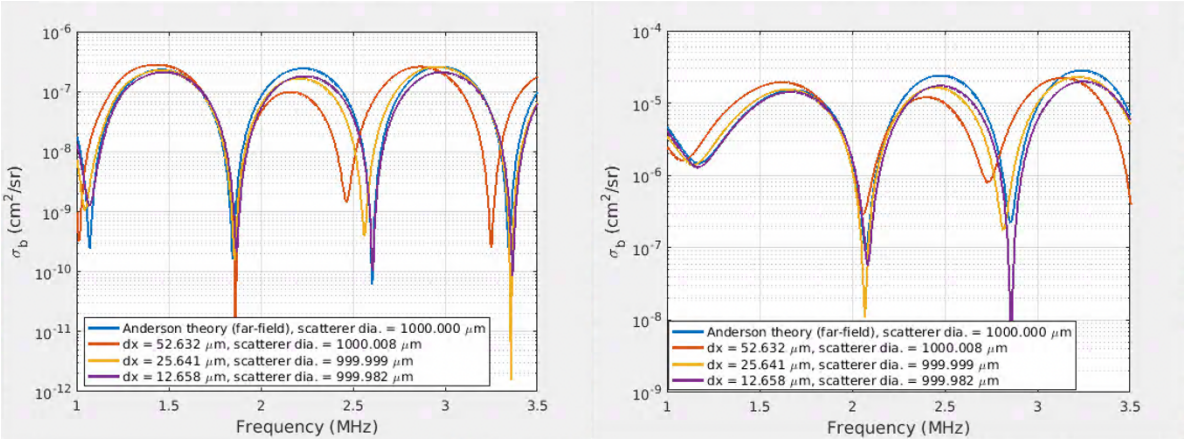

Fig. 4.7. Extracted differential backscatter cross-section for the *focused-transducer scheme* for (a) *weak scatterer* with 2% impedance contrast and (b) *strong scatterer* with 21% impedance contrast.

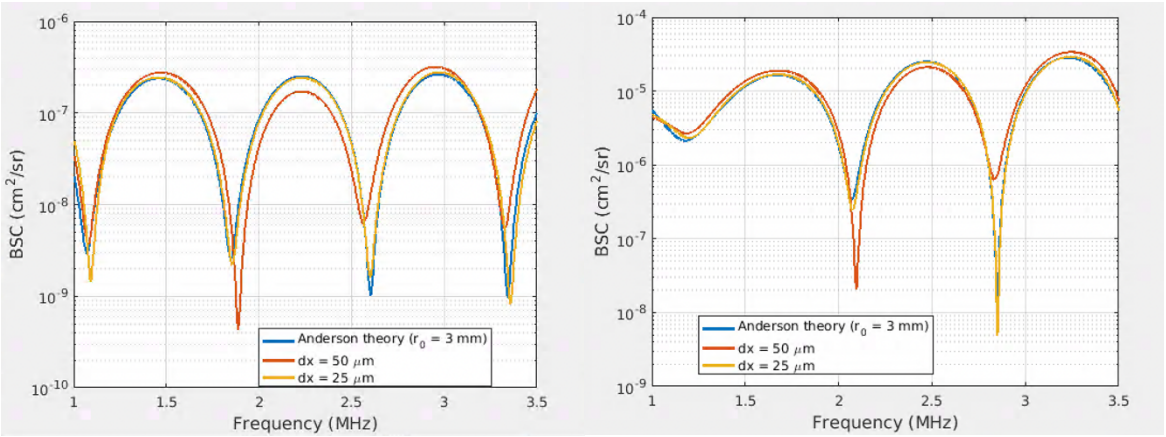

Fig. 4.8. Extracted differential backscatter cross-section for the *near-field scheme* for (a) *weak scatterer* with 2% impedance contrast and (b) *strong scatterer* with 21% impedance contrast.

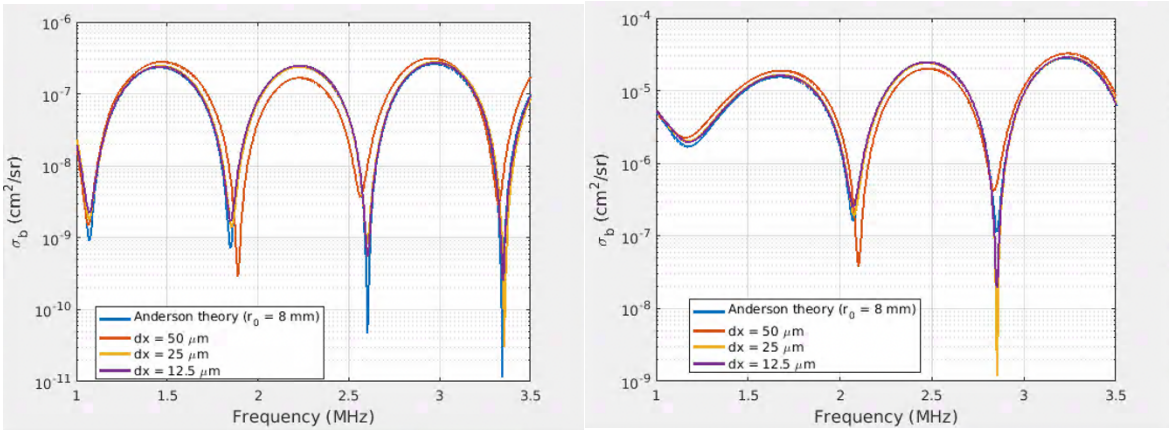

Fig. 4.9. Extracted differential backscatter cross-section for the *far-field scheme* for (a) *Weak scatterer* with 2% impedance contrast and (b) Strong scatterer with 21% impedance contrast.

Table 4.6. Extracted differential backscatter cross-section RMSE compared with Anderson theory

Scatterer	Backscatter parameter extraction schemes	dx ≈ 50 μm (cm^2/sr)	dx ≈ 25 μm (cm^2/sr)	dx ≈ 12.5 μm (cm^2/sr)	Anderson theory peak value (cm^2/sr)
Weak	Focused transducer	7.85E-08	3.06E-08	2.90E-08	2.64E-07
	Near-field	4.28E-08	8.43E-09	-	2.66E-07
	Far-field	4.30E-08	9.05E-09	4.49E-09	2.64E-07
Strong	Focused transducer	6.96E-06	3.50E-06	3.75E-06	2.86E-05
	Near-field	2.85E-06	5.07E-07	-	2.88E-05
	Far-field	2.78E-06	4.83E-07	3.53E-07	2.86E-05

4.5 Discussion

The *focused-transducer scheme* extended Kemmerer's work by modeling an experimental BSC extraction in k-Wave. Additionally, Chen's planar reference method was repurposed to extract the backscatter parameter of a single scatterer. While Kemmerer only extracted the normalized BSC, this work extracted the magnitude of the BSC. The extracted backscatter parameters from the *focused-transducer* scheme appeared to be less accurate than those extracted from other schemes, as observed in Figs. 4.7 – 4.9 and Table 4.6. This is because of the multiple sources of error in the *focused-transducer scheme* such as 1) finite transducer beamwidth comparable to scatterer, 2) non-planarity of the incident acoustic waves, 3) spatial discretization of the focused transducer, 4) averaging of the backscattered pressure over a wide solid angle instead of a small differential solid angle at $\theta = \pi$, and 5) spatial discretization of the scatterer. In contrast, the error in the *near-field* scheme could only be due to the scatterer spatial discretization. The sources of error in the *far-field* scheme are the non-planarity of the incident acoustic waves, the spatial discretization of the piston transmitter, and the scatterer spatial discretization. Generally, an increase in spatial resolution (or decrease in grid spacing) leads to better k-Wave simulation accuracy, as shown in Chapter 3. In Table 4.6, with decreasing grid spacing from 50 μm to 12.5 μm, the RMSE reduction was lesser for the *focused-transducer* scheme compared to the other two schemes. This observation indicates that transducer-related errors were the dominant sources of error in the *focused-transducer* scheme at lower grid spacings. Also, while the focused

transducer had a real-world counterpart, it was impractical from a simulation standpoint due to memory constraints. Hence, only a 2D axisymmetric simulation was performed for validation instead of the more generic 3D simulation.

To more directly evaluate the accuracy of k-Wave for scattering simulation, the *near-field* and *far-field* schemes were designed to eliminate the potential errors mentioned in the last paragraph. The *near-field* and *far-field* schemes implemented hypothetical transmitters and receivers. Additionally, they are free of diffraction and hence simplify the backscatter parameter extraction methodology. Among the two, the *near-field scheme* was the most precise, which can be concluded by a visual inspection of Figs. 4.8 and 4.9. This is because the wide planar transducer generated perfect plane waves in the *near-field* scheme. However, this scheme was not memory-efficient since it required planar transducers many times wider than the scatterer and, consequently, large computational domains. This is also the reason why dx = 12.5 μm was not simulated for the *near-field* scheme. Furthermore, at each relevant grid spacings, both schemes had similar RMS error values for the *weak scatterer* and the *strong scatterer*. So, the non-planarity of incident waves and the discretization of the piston transducer that was present in the *far-field* scheme but absent in the *near-field* scheme had minimal effect on the backscatter modeling. This observation also validates the design rules for the *far-field* scheme as given in Equations (4.21)-(4.23).

Ideally, a computational domain must not be too large compared to the single scatterer (or a 3DZM) while still satisfying the assumptions required to extract the backscatter parameters (plane wave incidence and far-field receiver). A large computational domain requires large (and often unrealistic) memory requirements in addition to a long run time. So, developing memory-efficient schemes for backscatter extraction is crucial, especially in iterative applications. The *far-field scheme* balances these conflicting requirements while providing good accuracy, as shown in Fig. 4.9. The extracted differential backscatter cross-section tracked the peaks and nulls of the theoretical Anderson curve. Also, the RMS error was less than 2% of the peak Anderson differential backscatter cross-section for both scatterers. This result shows that despite having approximate plane wave incidence, the *far-field scheme* extracted backscatter parameters accurately and efficiently. Hence, this method was also used for extracting the BSC of a collection of scatterers in Chapter 5. Furthermore, this scheme can be used in other acoustic simulation software and in more complicated scenarios such as with acoustic non-linearity, acoustic

attenuation, and shear waves to extract the exact backscatter parameters. Finally, in all these schemes, higher spatial resolution leads to higher accuracy as shown in Fig. 4.9. Hence, for a collection of scatterers, a preliminary simulation study must be conducted for the constituent single-scatterers. Such a study would find an optimum spatial resolution based on the bandwidth and accuracy requirements.

CHAPTER 5
SIMULATING ACOUSTIC BACKSCATTER FOR A COLLECTION OF SCATTERERS IN K-WAVE

5.1 Introduction

This chapter builds on the single scatterer simulation setup to simulate a collection of randomly and sparsely distributed scatterers. Such a 3DZM is simple and has a well-defined BSC that can be obtained by the incoherent scattering theory. The incoherent scattering BSC is a product of the single scatterer BSC in the same scattering volume and the number of scatterers. Hence it will be straightforward to validate the backscatter modeling and extraction in k-Wave and extend them to histology-based tissue 3DZMs. This chapter will also simulate backscatter from a collection of densely distributed scatterers in k-Wave. Due to dense packing, the positions of the scatterers are correlated that is captured by a quantity called structure function (SF). Consequently, the dense 3DZM displays coherent scattering and the BSC is a product of the single scatterer BSC in the same scattering volume, the number of scatterers, and the SF. Structure function has been shown to have a significant effect on scattering in aggregated red blood cells [43], [58], concentrated tissue-mimicking phantoms [42], concentrated cell pellet biophantoms [59], and many solid tumors [60], [61]. In the past, the SF simulations assumed a plane wave incidence in the entire medium, weak scattering, and absence of multiple scattering. Then, the structure function was calculated numerically by considering the scatterer position. In this study, however, the structure function of a collection of scatterers was modeled using full-wave simulations in k-Wave. The objective was to apply the k-Wave based backscatter modeling proposed in Chapter 4 in QUS simulations.

5.2 Acoustic scattering theory for a collection of spheres

Consider a medium of volume V composed of N identical scatterers irradiated with a plane wave of unit amplitude as shown in Fig. 5.1. Let the density and sound speed of the scatters be ρ and c, respectively. Let the density and sound speed of the background be ρ_0 and c_0, respectively.

By ignoring multiple scattering, the scattered pressure wave in the far-field can be expressed as (Eq. (4) of [62])

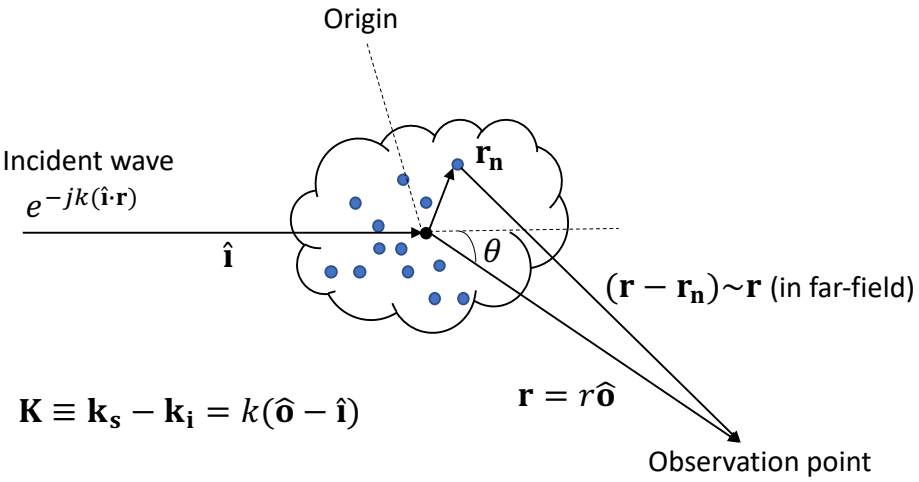

Fig. 5.1. Geometry illustrating the acoustic scattering from a single scatterer in the far-field.

$$p_s(\boldsymbol{r}) = \frac{e^{ikr}}{r}\sum_{n=1}^{N}\Phi_n(\mathbf{K})e^{i\mathbf{K}\cdot\mathbf{r_n}}\,, \tag{5.1}$$

where $\mathbf{r}$ is the observation point, $r = |\mathbf{r}|$, k is the wavenumber ($k = 2\pi f/c$, where f is the wave frequency and c is the medium sound speed), $\mathbf{r}_\mathrm{n}$ is the scatterer position of the nth scatterer, $\Phi_n(\mathbf{K})$ is the complex scattering amplitude of the nth scatterer for a scattering vector $\mathbf{K}$ given by $\mathbf{K} = 2ksin(\theta/2)(\hat{\mathbf{o}} - \hat{\mathbf{i}})$ for a scattering angle θ (θ for backscattering is π). The scattering amplitude Φ_n is a function of the scatterer size, shape, and acoustic properties. Now, the backscatter coefficient (BSC) for the scattering volume can be expressed from Eq. (4.2) as

$$\sigma_{bsc}(f) = \frac{1}{V}\left|\sum_{n=1}^{N}\Phi_\mathrm{n}(-2k\,\hat{\mathbf{i}})\,e^{-i\,2k\,(\hat{\mathbf{i}}\cdot\mathbf{r_n})}\right|^2\,. \tag{5.2}$$

For identical fluid spheres, Φ_n is same as Φ, the scattering amplitude for a constituent spherical scatterer which can be related to Anderson theory as highlighted in Chapter 4. Then, the BSC expression reduces to

$$\sigma_{bsc}(f) = \frac{1}{V}|\Phi(-2k\,\hat{\mathbf{i}})|^2\left|\sum_{n=1}^{N}e^{-i\,2k\,(\hat{\mathbf{i}}\cdot\mathbf{r_n})}\right|^2\,. \tag{5.3}$$

Interestingly, for a continuous scattering volume, the BSC has real physical significance. With weak scattering and absence of multiple scattering, the BSC can be expressed as the squared magnitude of the 3D spatial Fourier transform of the underlying acoustic impedance variation ($\gamma = -2(\rho c - \rho_0 c_0)/\rho c$) along the backscattering vector ($-2k\,\hat{\mathbf{i}}$) as (which is equivalent to Eq. (62) of [63])

$$\sigma_{bsc}(f) = \frac{k^4}{16\pi^2 V} \left| \iiint \gamma(\mathbf{r})\, e^{-i\,2k\,(\hat{\mathbf{i}}\cdot\mathbf{r})} \right|^2 . \tag{5.4}$$

Hence, previous work used a spatial FFT approach for extracting the 3DZM BSC. Now, if the scatterers are spatially randomly distributed, then the phase terms in the summation in an infinitely large volume can be assumed to be uncorrelated. Then, the resulting incoherent BSC is

$$\sigma_{bsc,incoherent}(f) = \frac{N}{V} |\Phi(-2k\,\hat{\mathbf{i}})|^2 . \tag{5.5}$$

Hypothetically, if the 3DZM had only one spherical scatterer, then the resulting BSC is

$$\sigma_{bsc,single}(f) = \frac{1}{V} |\Phi(-2k\,\hat{\mathbf{i}})|^2 , \tag{5.6}$$

and the incoherent BSC can be expressed as a function of the single scatterer BSC as

$$\sigma_{bsc,incoherent}(f) = N\, \sigma_{bsc,single}(f) . \tag{5.7}$$

While spatial randomness is a good assumption for media with low scatterer concentration (volume concentration < 10%), it breaks down for media with dense scatterer concentration [64]. This is because the scatterer positions and consequently the phase terms are correlated. This spatial correlation in the BSC expression is captured by the structure function as [64]

$$S(\mathbf{K}) = \frac{1}{N} \left| \sum_{n=1}^{N} e^{i\mathbf{K}\cdot\mathbf{r_n}} \right|^2 . \tag{5.8}$$

Combining, Equations (5.3), (5.6), and (5.8), the generalized expression for BSC is given by

$$\sigma_{bsc}(f) = N\, \sigma_{bsc,single}(f)\, S(f) . \tag{5.9}$$

The expected value of structure function for a sparse medium is unity from Eq. (5.7) and Eq. (5.9). Equations (5.1) – (5.9) assume plane wave incidence, weak scattering, and the absence of multiple

scattering in the medium. In contrast, the method proposed in this chapter transcends the scattering assumptions by using full-wave simulations. However, for validation purposes, the scatterers in the 3DZM were set to have weak to moderate impedance contrasts ($\Delta z/z_0 \leq 21\%$) compared to the background. Consequently, weak to moderate scattering was assumed in the medium, and hence Equations (5.1) – (5.10) are assumed to be approximately correct for the k-Wave simulations.

5.3 Methodology

The 3DZMs had a 192 μm (L) wide spherical volume wherein identical 20-μm (d) fluid spheres were suspended in water. The ratio $d/2L$ was kept low (~0.1) to minimize container effects on the extracted BSC and structure function [65]. The frequency bandwidth for analysis was chosen to be 10-80 MHz. The scatterer diameter (d) and frequency bandwidth were chosen to approximately mimic the BSC extraction of tumors in [64] wherein the mean radius of the scatterers ranged between 6.7-8.9 μm and the BSC was examined in 10-105 MHz. To observe the variation of BSC with impedance contrast, two sets of 3DZMs were simulated: 1) Set 1 had 3DZMs populated with *weak scatterer* with an acoustic impedance 2% higher than the background water and 2) Set 2 had 3DZMs populated with *strong scatterer* with an acoustic impedance 21% higher than the background water. Next, for a given volume concentration (h), the random positions of the scatterers were generated from a hard-sphere distribution which assumed no overlap between the spheres. One realization each was generated for a sparse medium (5% volume concentration) and a dense medium (50% volume concentration). The number of scatterers (N) in the sparse medium and the dense medium was 49 and 444 respectively. Overall, four 3DZMs of two impedance contrasts and two volume concentrations were simulated. Then, the goal of this section was to extract each 3DZM's radially averaged BSC using k-Wave.

First, single scatterer BSC was extracted for the *weak scatterer* and the *strong scatterer* using the *far-field scheme* as shown in Fig. 4.6. A spatial resolution (dx) of 2.5 μm produced reasonably accurate BSC in 10-80 MHz bandwidth while having a low run time and was adopted for the 3DZM simulations. The 3DZMs are assumed to be isotropic which is a common assumption in the study of homogenous tissues in QUS. Hence, the radially averaged BSC was calculated from multiple simulations of the given 3DZM. Each 3DZM was rotated with eight (M) equally spaced

angles from 0 to 180° along both X-axis and Y-axis. For the resulting 64 (M^2) 3DZM copies, the *far-field scheme* of backscatter extraction was applied along Z-axis as shown in Fig. 5.2. The setup was suitably designed to meet the rules in Equations (4.21)-(4.23). Equation (4.2) was applied to compute the BSC of each 3DZM copy. To be consistent with chapter 4, the scattering volume was assumed to be a cube with a width L ($V = L^3$). Finally, the acquired BSC was averaged across all the M^2 3DZM copies to generate the radially averaged BSC. The simulation and setup parameters for the single scatterer and a single 3DZM are summarized in Table 5.1 and Table 5.2, respectively.

Next, for the sparse 3DZMs, the theoretical BSC is calculated using Eq. (5.7) by assuming incoherent scattering. For the dense 3DZMs, the structure function was numerically calculated ($SF_{numerical}$) by applying Eq. (5.8), also in a radially averaged manner. Note that the dense 3DZMs had the same spatial distribution across impedance contrasts. Then, their corresponding theoretical BSC was calculated by applying Eq. (5.9).

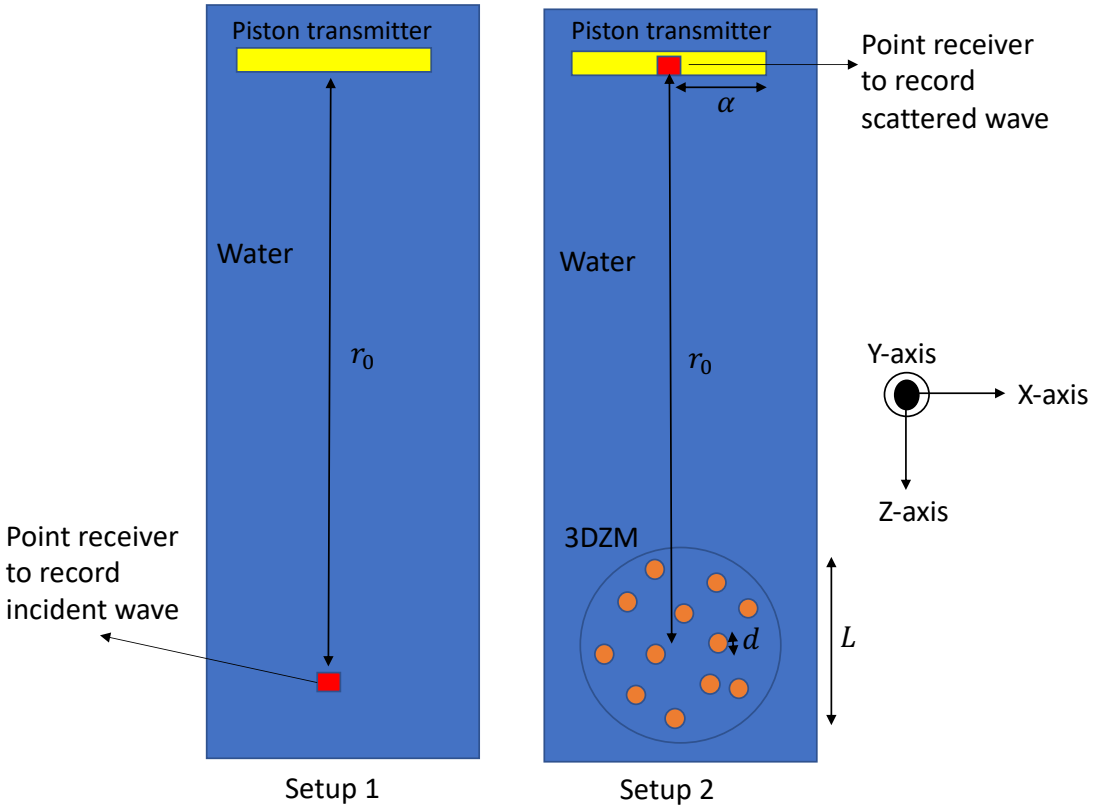

Fig. 5.2. Vertical cross-section of the *far-field scheme* to extract the exact BSC of a 3DZM.

Table 5.1. Simulation and setup parameters for extracting the BSC of a single scatterer

Parameters		Simulation	
Transducer	Radius (α)	10 μm	
	Center frequency	20 MHz, 60 MHz	
	3-dB Bandwidth	30%	
Scatterer	Scatterer diameter (d)	20 μm	
	Scatterer Sound speed	1495 m/s (w*eak scatterer*), 1628 m/s (*strong scatterer*)	
	Scatterer Density	1010 kg/m^3 (*weak scatterer*), 1100 kg/m^3 (*strong scatterer*)	
Background	Sound speed	1480 m/s	
	Density	1000 kg/m^3	
Other	r_0 (Distance between transmitter and scatterer)	400 μm	
Computational domain	Grid spacing (dx)	2.5 μm	1 μm
	Time step (dt)	0.38 ns	0.12 ns

Table 5.2 Simulation and setup parameters for extracting the BSC of a rotated 3DZM copy

Parameters		Simulation
Transducer	Radius (α)	50 μm
	Center frequency	20 MHz, 60 MHz
	3-dB Bandwidth	30%
3DZM	Width (L)	192 μm
	Scatterer diameter (d)	20 μm
	Scatterer Sound speed	1495 m/s (*weak scatterer*), 1628 m/s (*strong scatterer*)
	Scatterer Density	1010 kg/m^3 (*weak scatterer*), 1100 kg/m^3 (*strong scatterer*)
	Volume concentration	5%, 10%, 50%
Background	Sound speed	1480 m/s
	Density	1000 kg/m^3
Other	r_0 (Distance between transmitter and scatterer)	1.6 mm
Computational domain	Grid spacing (dx)	2.5 μm
	Time step (dt)	0.38 ns

5.4 Results

The extracted differential backscatter cross-section for the single scatterer simulations are plotted in Fig. 5.3. The extracted and averaged BSC for the rotated copies of the sparse 3DZM and the dense 3DZM are plotted in Fig. 5.4 and Fig. 5.5, respectively. In Figs. 5.4 and 5.5, the radially averaged BSC is compared with the Anderson BSC from the incoherent scattering theory. In Fig. 5.6, the radially averaged BSC of the dense 3DZM is compared with Anderson BSC from both incoherent and coherent scattering theory.

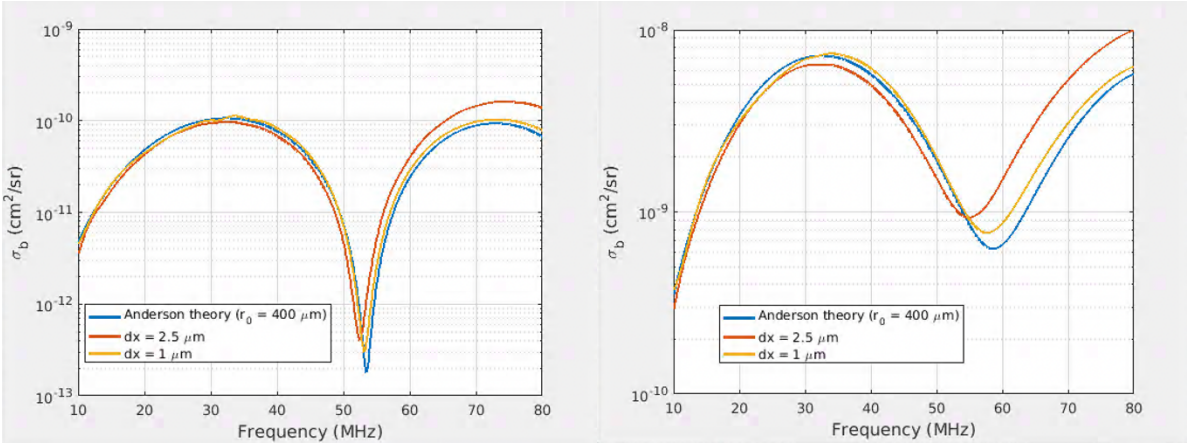

Fig. 5.3. Extracted differential backscatter cross-section for the single scatterer for (a) *weak scatterer* with 2% impedance contrast and (b) *strong scatterer* with 21% impedance contrast.

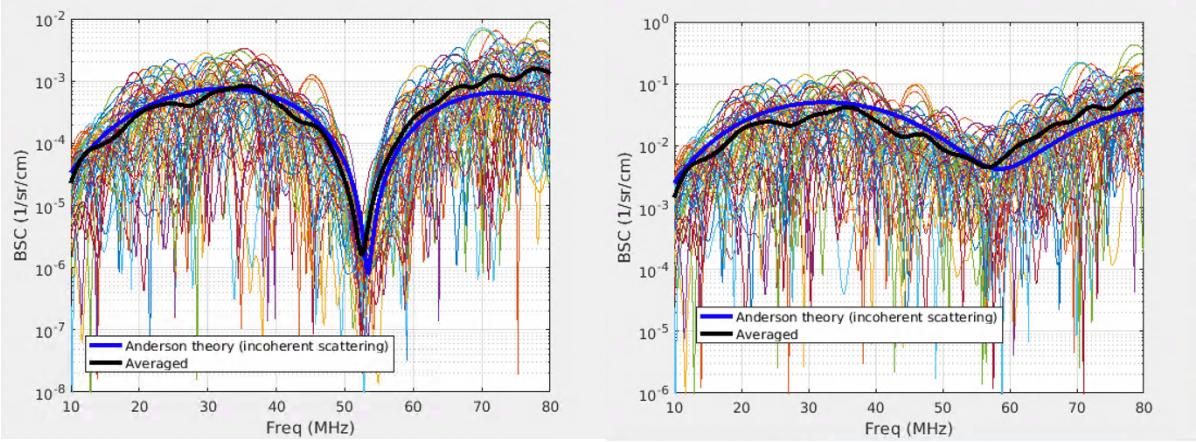

Fig. 5.4. Extracted and averaged BSC for 3DZMs with 5% volume concentration and 49 scatterers for (a) *weak scatterer* with 2% impedance contrast and (b) *strong scatterer* with 21% impedance contrast. The extracted BSC is compared with Anderson's theory for incoherent scattering (Eq. (5.7)). Spatial resolution (dx) = 2.5 µm.

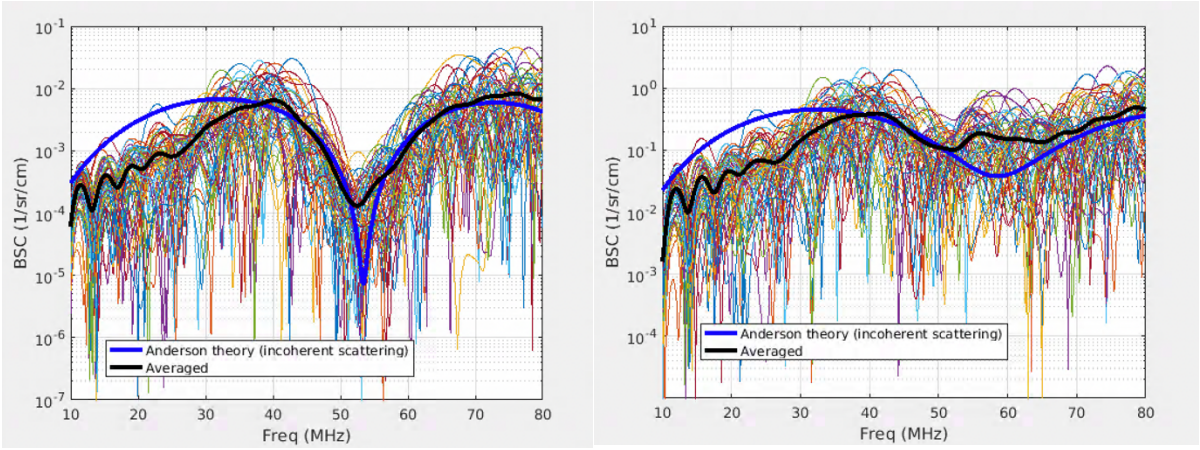

Fig. 5.5. Extracted and averaged BSC for 3DZMs with 50% volume concentration and 444 scatterers for (a) *weak scatterer* with 2% impedance contrast and (b) *strong scatterer* with 21% impedance contrast. The extracted BSC is compared with Anderson's theory for incoherent scattering (Eq. (5.7)). Spatial resolution (dx) = 2.5 μm.

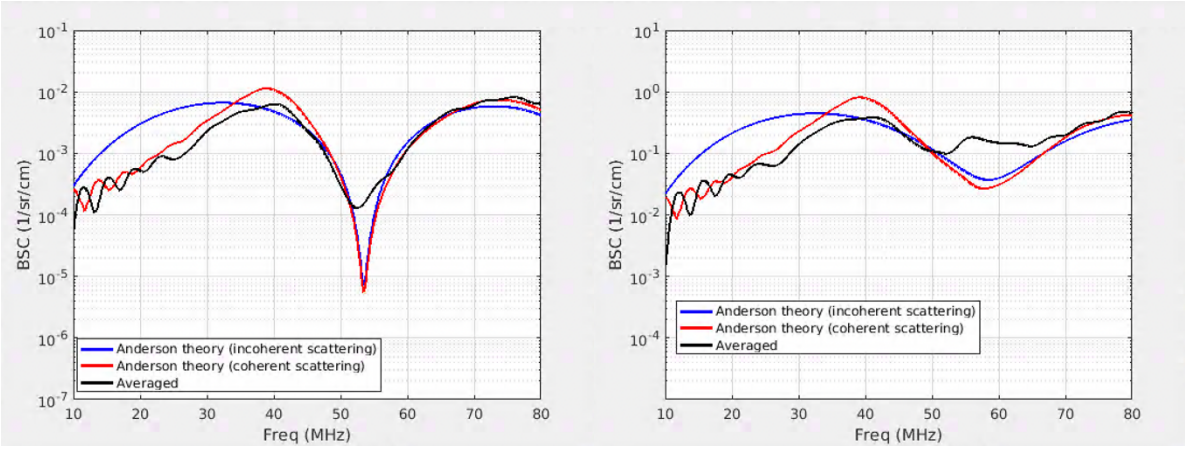

Fig. 5.6. Radially averaged BSC for 3DZMs with 50% volume concentration and 444 scatterers for (a) *weak scatterer* with 2% impedance contrast and (b) *strong scatterer* with 21% impedance contrast. The extracted BSC is compared with Anderson's theory for incoherent scattering (Eq. (5.7)) and coherent scattering (Eq. (5.9)). Spatial resolution (dx) = 2.5 μm.

5.5 Discussion

The radially averaged BSC for the sparse 3DZMs approximately matched the Anderson theory for incoherent scattering, as shown in Fig. 5.4. The small mismatch observed for the *strong*

scatterer at higher frequencies, as shown in Fig. 5.4(b), is due to insufficient spatial resolution. This mismatch is also observed in the single scatterer differential backscattering cross-section results for the *strong scatterer* in Fig.5.3(b). This result shows that the k-Wave modeling was accurate in simulating and extracting the BSC from a collection of spheres and in capturing the incoherent scattering from the sparse medium. In the future, this modeling and BSC extraction exercise can be implemented for the full-fledged 3DZM prepared from tissue histology.

Next, the radially averaged BSC for the dense 3DZMs did not match the Anderson BSC for incoherent scattering (Fig. 5.5) as expected. In contrast, the radially averaged BSC was closer to the Anderson BSC for coherent scattering (Fig. 5.6) albeit with a notable exception. Specifically, while there was good matching in 10-50 MHz between the acquired and theoretical BSC, there was a significant mismatch in 50-65 MHz for both the *weak scatterer* and the *strong scatterer*. This was because the dense 3DZM's BSC deviated from the coherent scattering theory at the nulls while the sparse 3DZM's BSC had good matching with the incoherent scattering theory at the nulls of the single scatterer BSC. Interestingly, this mismatch was observed for both impedance contrasts. So, the mismatch is possibly due to one of the following reasons: 1) It is an artifact of the setup, or the 'rotate and average' function applied on the 3DZM. 2) The scattering assumptions of plane wave incidence and the absence of multiple scattering were violated due to dense heterogeneity. Since the mismatch was present for both impedance contrasts, it was likely not caused by a violation of the weak scattering assumption.

In the future, the same 3DZM copies and the setup can be simulated using the Kemmerer method [7] in Field-II. Since Field-II uses the spatial impulse response method, assumptions of plane wave incidence and the absence of multiple scattering are built into the simulation method. If the mismatch disappears in the radially averaged BSC, then it can be concluded that the BSC obtained from k-Wave is accurate and is the result of a full-wave simulation that transcends the scattering assumptions. Such a result would be valuable and would build a strong case for full-wave simulations in studying acoustic structure function, especially in dense mediums. On the contrary, if the BSC mismatch persists in Field-II, then it is possibly an artifact of the setup or the rotation and averaging of 3DZMs. Then, techniques would have to be designed to eliminate these artifacts.

CHAPTER 6
IMPROVING SIMULATION ACCURACY BY APPLYING STAIRCASE-FREE DISCRETIZATION OF HETEROGENEOUS MEDIA

6.1 Motivation

As explained in Chapter 2, k-Wave adopts a discrete spatial and discrete temporal scheme to model acoustic wave propagation. When discretizing continuous media, the simulation accuracy improves with a higher spatial resolution (or smaller grid spacing). This improvement was observed in Chapter 3 for acoustic reflection and transmission and in Chapter 4 for acoustic scattering. However, the high spatial resolution also leads to large grid sizes and hence high computational cost. To navigate this dilemma, this chapter extends a method proposed by Wise et al. [66] to improve simulation accuracy even at low spatial resolutions. K-Wave relies on spatial FFT to compute the gradients of pressure and particle velocity in the wave equation. Hence, the discrete and finite spatial frequencies supported by a simulation form the basis functions $\mathcal{B}$ for expressing all spatial objects. Wise et al. showed that while discretizing a continuous source object, a projection onto $\mathcal{B}$ produces a more accurate simulation as opposed to a simple rectangular grid sampling. They applied this staircase-free technique to discretize sources and sensors. This chapter builds on their work to show that for linear wave propagation, the staircase-free technique can be applied to the discretization of sound speed and density maps as well. Specifically, staircase-free discretization was applied to continuous 3DZMs to improve the accuracy of the simulated backscatter at low spatial resolutions.

6.2 Theory

The wave equations in k-Wave for linear wave propagation in an attenuative medium are given in Equations (2.1) – (2.3) [23]. However, for a non-attenuative medium assumed in Chapters 4 and 5, pressure-density relation is given by

$$p = c_0^2 \rho \ . \tag{6.1}$$

By combining Equations (2.1), (2.2), and (6.1), the wave equation is represented as

$$\nabla^2 p - \frac{1}{c_0^2}\frac{\partial^2 p}{\partial t^2} = \rho_0 \nabla \cdot \boldsymbol{S_F} - \frac{\partial}{\partial t} S_M \ . \tag{6.2}$$

In Equations (2.1), (2.2), and (6.2), the wave equation is linear with the source terms $\boldsymbol{S_F}$ and S_M. This statement remains true for non-linear wave propagation and attenuative media. Hence, one interpretation of the staircase-free method is to perform spatial anti-alias filtering of continuous source objects before rectangular discretization. The continuous source objects would have infinite spatial frequency support, whereas the support of the filtered object would be $\mathcal{B}$. On the contrary, the linear wave equation cannot be considered linear with the density map (ρ_0) and the sound speed map (c_0) because of the $1/\rho_0$ term in Eq. (2.1) and the c_0^2 term in Eq. (6.1). However, for small variations in sound speed and density map, the linear wave equation can be considered to be linear with $\Delta\rho_0/\rho_0$ and $\Delta c_0/c_0$ akin to small-signal analysis in circuit theory. Hence, the staircase-free discretization can be extended to impedance maps with small variations for linear wave propagation. However, this assumption will break down for non-linear wave propagation and attenuative media due to a more complicated wave equation.

Although Wise et al. discuss different ways of applying the staircase-free discretization, in this work, the spatial FFT-based anti-alias filtering approach will be used. This approach will be illustrated with the discretization of a continuous 2D object, a circle, with a spatial resolution of dx. The traditional k-Wave scheme discretizes the circle at the rectangular grid points as shown in Fig. 6.1. In other words, a continuous circle was spatially sampled at a rectangular spatial frequency $(k_u, k_v) = (1/dx, 1/dx) = (k_0, k_0)$, implying that the Nyquist spatial frequency is $(k_0/2, k_0/2)$. However, since there was no anti-alias filtering performed, the baseband signal (2D circle in this case) would be distorted by the aliased content from higher frequencies. This distortion in the baseband signal would lead to distortions in the acquired BSC results as well.

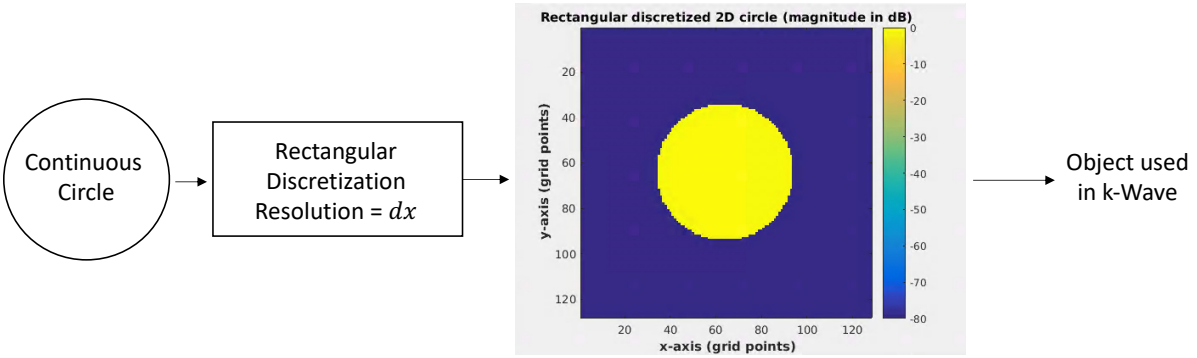

Fig. 6.1. Traditional rectangular discretization scheme in k-Wave.

In staircase-free discretization, the circle was rectangularly pre-sampled at a M-times higher spatial frequency (dx/M spatial resolution) as shown in Fig. 6.2. Then, spatial FFT was applied to convert the pre-sampled circle to spatial-frequency domain. Next, this spatial-frequency representation was filtered within a square region such that $|k_u|, |k_v| < k_0/2$. Finally, inverse spatial-FFT was applied and then rectangularly resampled with a spatial resolution of dx. This process ensures that the following spatial frequency ranges ($k_0/2 < |k_u|, |k_v| < Mk_0/2$) are not aliased into baseband.

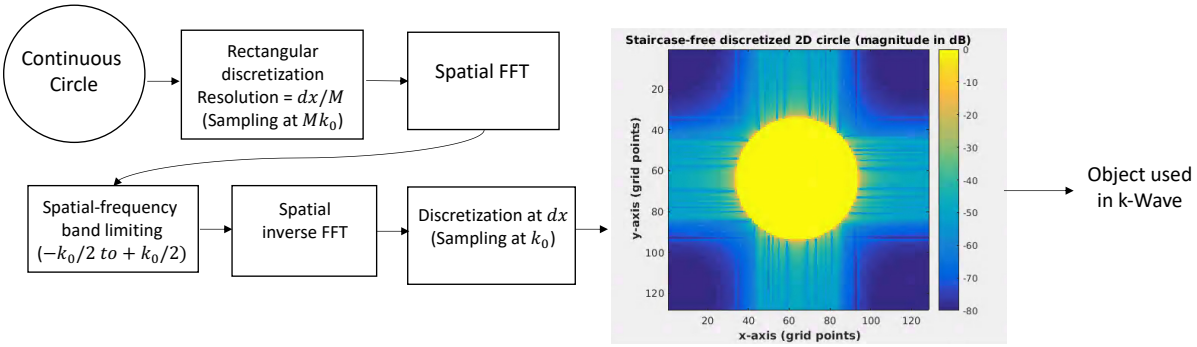

Fig. 6.2. Staircase-free discretization scheme with an up-sampling factor of M in k-Wave.

6.3 Methodology

To validate that the staircase-free discretization approach works for discretizing speed of sound and density maps, the approach was applied on a 1 mm single fluid scatterer for a spatial resolution (dx) of 100 μm. Three impedance contrasts ($\Delta z/z_0$) of 2%, 21%, and 125% were staircase-free discretized and rectangularly discretized, and the differential backscatter cross-section was extracted using the far-field scheme as shown in Fig. 4.6 in a 1.0-3.5 MHz frequency bandwidth. RMS error values were also calculated for these results by comparison with Anderson's theory as per Eq. (4.24). The setup parameters (d, α, and r_0) were the same as Chapter 4, as summarized in Table 4.1. For a fluid scatterer, impedance contrast of 125% was unrealistic and typically would have to support shear waves. However, 3D elastic simulations in k-Wave also use the spatial FFT approach. Hence this test was intended to prove the efficacy of staircase-free discretization in any future linear elastic k-Wave simulations.

Next, staircase-free discretization was applied on the 192 μm sparse 3DZM with a 5% volume concentration and populated with 20 μm scatterers from Chapter 5. A spatial resolution of 2.5 μm was used in this test. Two impedance contrasts ($\Delta z/z_0$) of 2% and 21% were staircase-free discretized and rectangularly discretized, and the radially averaged BSC were extracted using the *far-field scheme* as shown in Fig. 5.2 in a 10-80 MHz frequency bandwidth. The setup parameters (L, d, α, and r_0) were the same as Chapter 5 and are summarized in Table 5.1. An 8x pre-sampling was followed in the discretization of both the single scatterer and the 3DZM.

6.4 Results

The differential backscatter cross-section results for the 1 mm single scatterer are plotted in Fig. 6.3 for the traditional and staircase-free discretization and compared with the theoretical Anderson differential backscatter cross-section. The corresponding RMS error values are tabulated in Table 6.1. Next, the radially averaged BSC results from the sparse 3DZMs are plotted in Fig. 6.4 for the rectangular and the staircase-free discretization and compared with the Anderson BSC [50] for incoherent scattering.

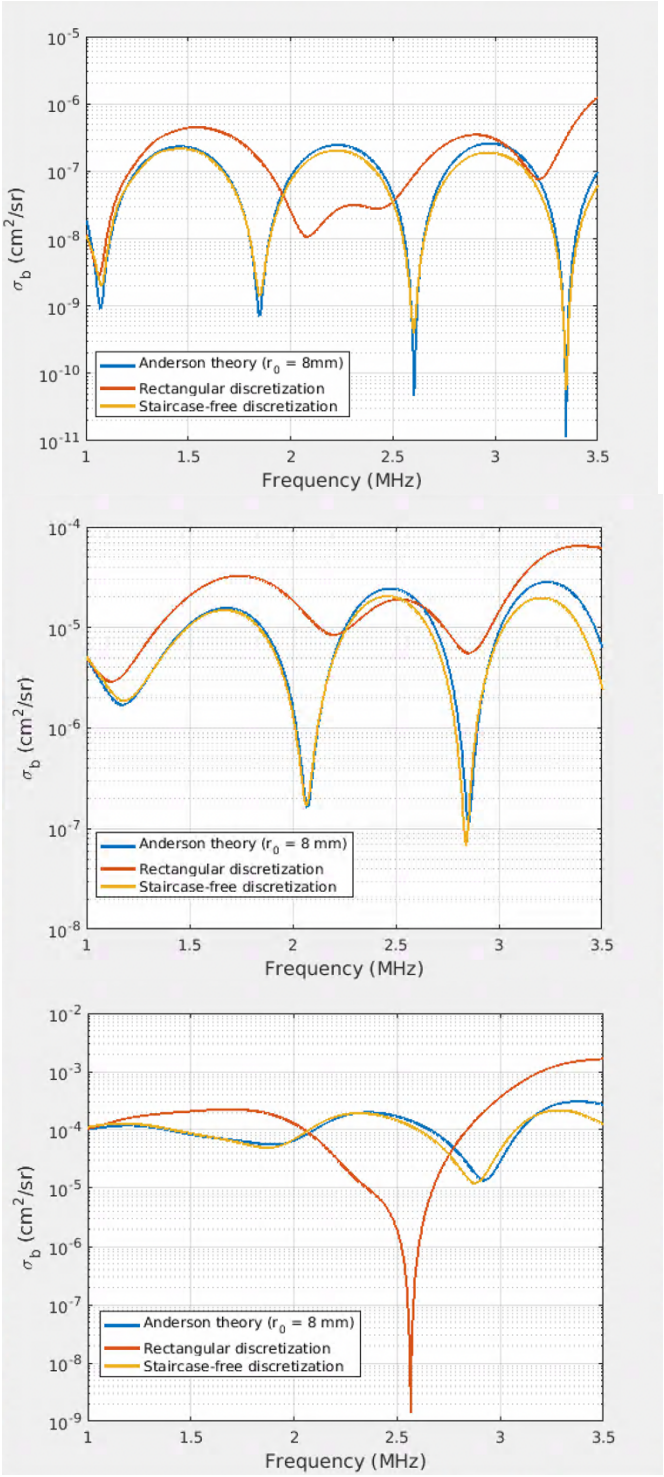

Fig. 6.3. Extracted differential backscatter cross-section for rectangular and staircase-free discretization compared with Anderson theory for an impedance contrast of (a) 2% (b) 21% and (c) 125%. Spatial resolution (dx) = 100 μm, scatterer diameter = 1 mm.

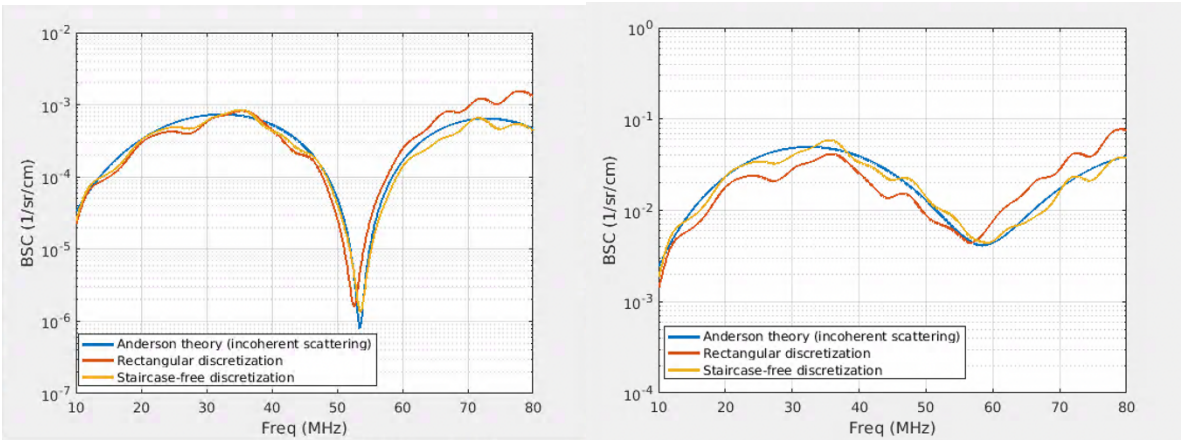

Fig. 6.4. Radially averaged BSC of the sparse 3DZM (h = 5%, N = 49) for rectangular and staircase-free discretization compared with Anderson theory for an impedance contrast of (a) 2% and (b) 21%. Spatial resolution (dx) = 2.5 µm, scatterer diameter = 20 µm, and 3DZM width = 192 µm.

Table 6.1. Extracted differential backscatter cross-section's RMSE ($\sigma_{b,RMSE}$) compared with Anderson's theory for the single scatterer simulations

Relative impedance contrast	Anderson BSC (peak value) (cm^2/sr)	$\sigma_{b,RMSE}$ (cm^2/sr)		$\sigma_{b,RMSE}$ / max $\sigma_{b,Anderson}$ (%)	
		Rectangular discretization	Staircase-free discretization	Rectangular discretization	Staircase-free discretization
2%	2.64E-07	2.38E-07	2.84E-08	90.1	10.8
21%	2.86E-05	1.74E-05	3.53E-06	60.9	12.3
125%	3.13E-04	4.51E-04	3.88E-05	143.9	12.4

6.5 Discussion

As shown in Fig. 6.3, staircase-free discretization was able to significantly improve the accuracy of backscatter results at a low spatial resolution of 100 µm. Additionally, the staircase-free discretization was also shown to be effective for 3DZMs as shown in Fig. 6.4. These results show that for frequency bandwidths lower than spatial Nyquist, staircase-free discretization of continuous media can ensure accurate backscatter simulations. The staircase-free discretization can be especially useful when faced with simulation memory constraints. For instance, discrete histology-based tissue 3DZMs can be spatially down-sampled using the staircase-free approach if

the bandwidth of interest is much lower than the spatial Nyquist. The down-sampling can then lead to smaller grid sizes and consequently lower memory and run time.

However, there are some limitations to the staircase-free approach. First, it will work well for low to moderate impedance contrasts ($\Delta z/z_0$ < 20%, such as those observed in soft tissues) but may not work for high impedance contrasts ($\Delta z/z_0$ > 100%) as explained in section 6.2. However, this limitation does not affect the simulation of scattering in soft tissues. Second, this technique may not work for non-linear wave propagation and in attenuative media, as highlighted in section 6.2. Finally, the higher spatial sampling of continuous objects requires large grids, often leading to prohibitively large memory requirements and pre-processing time. For instance, say a rectangular grid has a simulation time of T seconds/time-step and memory requirement of MEM in a computing system. Then, an 8x pre-sampling in the same system will roughly have a pre-processing time of 8^3T seconds for implementing the FFT-IFFT step in staircase correction. However, a more stringent limitation is the memory requirement which would approximately be $8^3MEM/25 \approx 20MEM$. Factor 25 in the denominator occurs due to the peculiarity of the implementation of rectangular grids in k-Wave (see Eq. (4.1) in [23]).

CHAPTER 7
CONCLUSIONS AND FUTURE WORK

7.1 Conclusions

In this work, k-Wave was successfully applied in two different QUS applications – to model planar acoustic reflection and transmission in Part 1, and to model acoustic backscatter from fluid scatterers in Part 2.

In Part 1, a novel and simple method capable of simultaneously measuring phantom attenuation coefficient (AC) and surface membrane transmission loss was proposed. Then, it was validated to be accurate and precise, experimentally and in k-Wave simulation. In contrast to the experimental validation, k-Wave allowed programming of the phantom properties. Hence, the method's accuracy could be quantified by comparing acquired phantom AC with the ground truth.

Part 2 accurately modeled linear acoustic scattering from a single fluid scatterer and a sparsely distributed collection of monodisperse fluid scatterers for plane wave incidence in k-Wave. The exact, diffraction-free backscatter coefficient (BSC) was acquired for both cases and validated by comparing with the Anderson theory for the single scatterer and with the incoherent scattering theory for the scatterer collection. In the process, the Chen method [1] of extracting the BSC of a random medium using a planar reference was modified to suit a single scatterer. Additionally, the staircase-free representation of sources proposed by Wise et al. [66] was extended to the heterogeneous simulation medium, significantly reducing the computational requirements for simulating single scatterers and the scatterer collection. Finally, BSC was acquired for a densely distributed collection of monodisperse fluid spheres and compared with structure function (SF) theory. The acquired BSC matched structure function theory at lower frequencies but significantly diverged at nulls of the single scatterer BSC. Interestingly, this artifact was not observed for the sparse medium simulation and must be examined more closely in future research studies.

7.2 Future work

As highlighted in Chapter 3, the incident acoustic waves for the weakly focused transducers are only approximately planar. Hence, the phantom AC measurement can be improved with diffraction correction. A closed-form analysis of this effect is complicated. Instead, a simulation in k-Wave is ideal for this exploration since it allows the user to visualize and quantify the incident and reflected waves. So, it would be possible to implement either an approximate or an empirical diffraction correction.

The study of acoustic scattering in k-Wave can be first extended to non-linear and elastic wave propagation supported by the tool. Such an exercise will be valuable in QUS research related to bones, skull, harmonic imaging, contrast microbubble imaging, among others. Next, the BSC and structure function artifacts observed for the dense monodisperse medium in k-Wave must be further examined. Moving towards realistic cases, the full-wave scattering simulations in k-Wave can be extended to polydisperse distributions and tissue histology-based 3D impedance maps (3DZM). By leveraging the full-wave simulation results, such an exploration in k-Wave can lead to many innovations in QUS such as 1) development of better scattering models leading to better detection and estimation, 2) training of learning networks that implement model-free detection and estimation, and 3) experimentation and development of transducer architectures and excitation schemes specific to a given QUS application. Finally, the limits of staircase-free discretization must be explored across grid sizes, spatial resolution, pre-sampling factor, impedance contrast, and medium attenuation.

REFERENCES

[1] X. Chen, D. Phillips, K. Q. Schwarz, J. G. Mottley, and K. J. Parker, "The measurement of backscatter coefficient from a broadband pulse-echo system: a new formulation," *IEEE Trans Ultrason Ferroelectr Freq Control*, vol. 44, no. 2, pp. 515–525, 1997, doi: 10.1109/58.585136.

[2] D. Baek, O. Oralkan, M. Kupnik, M. Willatzen, B. T. Khuri-Yakub, and J. A. Jensen, "Simulating capacitive micromachined ultrasonic transducers (CMUTs) using field II," in *2010 IEEE International Ultrasonics Symposium*, San Diego, CA, Oct. 2010, pp. 439–442. doi: 10.1109/ULTSYM.2010.5935580.

[3] P. B. Rosnitskiy, P. V. Yuldashev, O. A. Sapozhnikov, L. R. Gavrilov, and V. A. Khokhlova, "Simulation of nonlinear trans-skull focusing and formation of shocks in brain using a fully populated ultrasound array with aberration correction," *J Acoust Soc Am*, vol. 146, no. 3, p. 1786, Sep. 2019, doi: 10.1121/1.5126685.

[4] V. Amin, L. Wu, T. Long, R. Roberts, S. McClure, and T. Ryken, "Therapy planning and monitoring of tissue ablation by high intensity focused ultrasound (HIFU) using imaging and simulation," *Annu Int Conf IEEE Eng Med Biol Soc*, vol. 2008, p. 4471, 2008, doi: 10.1109/IEMBS.2008.4650204.

[5] A. Grisey, S. Yon, V. Letort, and P. Lafitte, "Simulation of high-intensity focused ultrasound lesions in presence of boiling," *J Ther Ultrasound*, vol. 4, p. 11, 2016, doi: 10.1186/s40349-016-0056-9.

[6] G. Pinton, J.-F. Aubry, M. Fink, and M. Tanter, "Effects of nonlinear ultrasound propagation on high intensity brain therapy: Nonlinear ultrasound propagation and high intensity brain therapy," *Med. Phys.*, vol. 38, no. 3, pp. 1207–1216, Feb. 2011, doi: 10.1118/1.3531553.

[7] J. P. Kemmerer, M. L. Oelze, and M. Gyöngy, “Scattering by single physically large and weak scatterers in the beam of a single-element transducer,” *J Acoust Soc Am*, vol. 137, no. 3, pp. 1153–1163, Mar. 2015, doi: 10.1121/1.4913781.

[8] K. J. Parker and S. S. Poul, “Speckle from branching vasculature: dependence on number density,” *J. Med. Imag.*, vol. 7, no. 02, p. 1, Apr. 2020, doi: 10.1117/1.JMI.7.2.027001.

[9] H. Song, U. Woo, and H. Choi, “Numerical Analysis of Ultrasonic Multiple Scattering for Fine Dust Number Density Estimation,” *Applied Sciences*, vol. 11, no. 2, p. 555, Jan. 2021, doi: 10.3390/app11020555.

[10] M. J. Santos and J. B. Santos, “Ultrasonic Scattering Attenuation in Nodular Cast Iron: Experimental and Simulation Studies,” *SV-JME*, vol. 67, no. 5, pp. 245–255, May 2021, doi: 10.5545/sv-jme.2020.7078.

[11] M. D. Verweij, Bradley E. Treeby, K. W. A Van Dongen, and L Demi, “Simulation of ultrasound fields,” in *Comprehensive biomedical physics*, 2014, pp. 465–499.

[12] D. Garcia, “SIMUS: an open-source simulator for ultrasound imaging. Part I: theory & examples,” *arXiv:2102.02738 [physics]*, Sep. 2021, Accessed: Nov. 15, 2021. [Online]. Available: http://arxiv.org/abs/2102.02738

[13] Jørgen Arendt Jensen, “A model for the propagation and scattering of ultrasound in tissue,” *The Journal of the Acoustical Society of America*, vol. 89, no. 1, pp. 182–190, Jan. 1991, doi: 10.1121/1.400497.

[14] J. A. Jensen and N. B. Svendsen, “Calculation of pressure fields from arbitrarily shaped, apodized, and excited ultrasound transducers,” *IEEE Trans. Ultrason., Ferroelect., Freq. Contr.*, vol. 39, no. 2, pp. 262–267, Mar. 1992, doi: 10.1109/58.139123.

[15] J. A. Jensen, “Field: A Program for Simulating Ultrasound Systems,” *Medical & Biological Engineering & Computing*, vol. 34, no. sup. 1, pp. 351–353, 1996.

[16] G. E. Tupholme, “Generation of acoustic pulses by baffled plane pistons,” *Mathematika*, vol. 16, no. 2, pp. 209–224, Dec. 1969, doi: 10.1112/S0025579300008184.

[17] P. R. Stepanishen, “Transient Radiation from Pistons in an Infinite Planar Baffle,” *The Journal of the Acoustical Society of America*, vol. 49, no. 5B, pp. 1629–1638, May 1971, doi: 10.1121/1.1912541.

[18] B. E. Treeby and B. T. Cox, “k-Wave: MATLAB toolbox for the simulation and reconstruction of photoacoustic wave fields,” *J. Biomed. Opt.*, vol. 15, no. 2, p. 021314, 2010, doi: 10.1117/1.3360308.

[19] B. E. Treeby, J. Jaros, A. P. Rendell, and B. T. Cox, “Modeling nonlinear ultrasound propagation in heterogeneous media with power law absorption using a k-space pseudospectral method,” *J Acoust Soc Am*, vol. 131, no. 6, pp. 4324–4336, Jun. 2012, doi: 10.1121/1.4712021.

[20] B. E. Treeby, J. Jaros, D. Rohrbach, and B. T. Cox, “Modelling elastic wave propagation using the k-Wave MATLAB Toolbox,” in *2014 IEEE International Ultrasonics Symposium*, Chicago, IL, USA, Sep. 2014, pp. 146–149. doi: 10.1109/ULTSYM.2014.0037.

[21] B. Treeby, F. Vaverka, and J. Jaros, “Performance and accuracy analysis of nonlinear k-Wave simulations using local domain decomposition with an 8-GPU server,” Santa Fe, New Mexico, USA, 2018, p. 022002. doi: 10.1121/2.0000883.

[22] J. Jaros, F. Vaverka, and B. E. Treeby, “Spectral Domain Decomposition Using Local Fourier Basis: Application to Ultrasound Simulation on a Cluster of GPUs,” *JSFI*, vol. 3, no. 3, Nov. 2016, doi: 10.14529/jsfi160305.

[23] B. E. Treeby, B. Cox, and J. Jaros, “k-Wave, a MATLAB toolbox for the time domain simulation of acoustic wave fields. User Manual (version 1.1).” Aug. 27, 2016. Accessed: Jun. 01, 2020. [Online]. Available: http://www.k-wave.org/manual/k-wave_user_manual_1.1.pdf

[24] J. L. B. Robertson, B. T. Cox, J. Jaros, and B. E. Treeby, “Accurate simulation of transcranial ultrasound propagation for ultrasonic neuromodulation and stimulation,” *J. Acoust. Soc. Am.*, vol. 141, no. 3, pp. 1726–1738, Mar. 2017, doi: 10.1121/1.4976339.

[25] K. A. Wear *et al.*, “Interlaboratory Comparison of Ultrasonic Backscatter Coefficient Measurements From 2 to 9 MHz,” *Journal of Ultrasound in Medicine*, vol. 24, no. 9, pp. 1235–1250, Sep. 2005, doi: 10.7863/jum.2005.24.9.1235.

[26] A. Han, M. P. Andre, J. W. Erdman, R. Loomba, C. B. Sirlin, and W. D. O’Brien, “Repeatability and Reproducibility of a Clinically Based QUS Phantom Study and Methodologies,” *IEEE Trans. Ultrason., Ferroelect., Freq. Contr.*, vol. 64, no. 1, pp. 218–231, Jan. 2017, doi: 10.1109/TUFFC.2016.2588979.

[27] K. Nagabhushana, W. D. O’Brien, and A. Han, “Technique to compensate for unknown laminate transmission loss in phantom attenuation measurements,” in *2020 IEEE International Ultrasonics Symposium (IUS)*, Las Vegas, NV, USA, Sep. 2020, pp. 1–4. doi: 10.1109/IUS46767.2020.9251582.

[28] B. S. Garra, M. F. Insana, T. H. Shawker, R. F. Wagner, M. Bradford, and M. A. Russell, “Quantitative Ultrasonic Detection and Classification of Diffuse Liver Disease Comparison with Human Observer Performance,” *Investigative Radiology*, vol. 24, no. 3, pp. 196–203, Mar. 1989, doi: 10.1097/00004424-198903000-00004.

[29] S. C. Lin *et al.*, “Noninvasive Diagnosis of Nonalcoholic Fatty Liver Disease and Quantification of Liver Fat Using a New Quantitative Ultrasound Technique,” *Clin Gastroenterol Hepatol*, vol. 13, no. 7, pp. 1337-1345.e6, Jul. 2015, doi: 10.1016/j.cgh.2014.11.027.

[30] A. Han *et al.*, “Assessment of Hepatic Steatosis in Nonalcoholic Fatty Liver Disease by Using Quantitative US,” *Radiology*, vol. 295, no. 1, pp. 106–113, Apr. 2020, doi: 10.1148/radiol.2020191152.

[31] M. F. Insana, T. J. Hall, J. G. Wood, and Z.-Y. Yan, “Renal Ultrasound Using Parametric Imaging Techniques to Detect Changes in Microstructure and Function,” *Investigative Radiology*, vol. 28, no. 8, pp. 720–725, Aug. 1993, doi: 10.1097/00004424-199308000-00013.

[32] E. J. Feleppa *et al.*, “Typing of prostate tissue by ultrasonic spectrum analysis,” *IEEE Trans. Ultrason., Ferroelect., Freq. Contr.*, vol. 43, no. 4, pp. 609–619, Jul. 1996, doi: 10.1109/58.503779.

[33] E. J. Feleppa, F. L. Lizzi, D. J. Coleman, and M. M. Yaremko, “Diagnostic spectrum analysis in ophthalmology: a physical perspective,” *Ultrasound Med Biol*, vol. 12, no. 8, pp. 623–631, Aug. 1986, doi: 10.1016/0301-5629(86)90183-3.

[34] F. T. H. Yu, E. Franceschini, B. Chayer, J. K. Armstrong, H. J. Meiselman, and G. Cloutier, “Ultrasonic parametric imaging of erythrocyte aggregation using the structure factor size estimator,” *Biorheology*, vol. 46, no. 4, pp. 343–363, 2009, doi: 10.3233/BIR-2009-0546.

[35] L. E. Kinsler, A. R. Frey, A. B. Coppens, and J. V. Sanders, *Fundamentals of Acoustics*, 4th ed. New York: Wiley, 2000.

[36] J. Lubbers and R. Graaff, “A simple and accurate formula for the sound velocity in water,” *Ultrasound Med Biol*, vol. 24, no. 7, pp. 1065–1068, Sep. 1998, doi: 10.1016/s0301-5629(98)00091-x.

[37] F. H. Fisher and V. P. Simmons, “Sound absorption in sea water,” *The Journal of the Acoustical Society of America*, vol. 62, no. 3, pp. 558–564, Sep. 1977, doi: 10.1121/1.381574.

[38] I. Y. Kuo, B. Hete, and K. K. Shung, “A novel method for the measurement of acoustic speed,” *J Acoust Soc Am*, vol. 88, no. 4, pp. 1679–1682, Oct. 1990, doi: 10.1121/1.400242.

[39] Altuglas International, “Plexiglas® general information and physical properties.” Accessed: Apr. 07, 2021. [Online]. Available: https://www.plexiglas.com/export/sites/plexiglas/.content/medias/downloads/sheet-docs/plexiglas-general-information-and-physical-properties.pdf

[40] M. L. Oelze and J. Mamou, “Review of Quantitative Ultrasound: Envelope Statistics and Backscatter Coefficient Imaging and Contributions to Diagnostic Ultrasound,” *IEEE Trans. Ultrason., Ferroelect., Freq. Contr.*, vol. 63, no. 2, pp. 336–351, Feb. 2016, doi: 10.1109/TUFFC.2015.2513958.

[41] D. C. Sullivan *et al.*, "Metrology Standards for Quantitative Imaging Biomarkers," *Radiology*, vol. 277, no. 3, pp. 813–825, Dec. 2015, doi: 10.1148/radiol.2015142202.

[42] E. Franceschini and R. Guillermin, "Experimental assessment of four ultrasound scattering models for characterizing concentrated tissue-mimicking phantoms," *J Acoust Soc Am*, vol. 132, no. 6, pp. 3735–3747, Dec. 2012, doi: 10.1121/1.4765072.

[43] E. Franceschini, R. K. Saha, and G. Cloutier, "Comparison of three scattering models for ultrasound blood characterization," *IEEE Trans. Ultrason., Ferroelect., Freq. Contr.*, vol. 60, no. 11, pp. 2321–2334, Nov. 2013, doi: 10.1109/TUFFC.2013.6644736.

[44] M. L. Oelze, W. D. O'Brien, J. P. Blue, and J. F. Zachary, "Differentiation and characterization of rat mammary fibroadenomas and 4T1 mouse carcinomas using quantitative ultrasound imaging," *IEEE Trans Med Imaging*, vol. 23, no. 6, pp. 764–771, Jun. 2004, doi: 10.1109/tmi.2004.826953.

[45] M. L. Oelze and W. D. O'Brien, "Application of three scattering models to characterization of solid tumors in mice," *Ultrason Imaging*, vol. 28, no. 2, pp. 83–96, Apr. 2006, doi: 10.1177/016173460602800202.

[46] M. L. Oelze and J. F. Zachary, "Examination of cancer in mouse models using high-frequency quantitative ultrasound," *Ultrasound Med Biol*, vol. 32, no. 11, pp. 1639–1648, Nov. 2006, doi: 10.1016/j.ultrasmedbio.2006.05.006.

[47] M. F. Insana, T. J. Hall, and J. L. Fishback, "Identifying acoustic scattering sources in normal renal parenchyma from the anisotropy in acoustic properties," *Ultrasound Med Biol*, vol. 17, no. 6, pp. 613–626, 1991, doi: 10.1016/0301-5629(91)90032-r.

[48] J. Mamou, M. L. Oelze, W. D. O'Brien, and J. F. Zachary, "Identifying ultrasonic scattering sites from three-dimensional impedance maps," *J Acoust Soc Am*, vol. 117, no. 1, pp. 413–423, Jan. 2005, doi: 10.1121/1.1810191.

[49] J. Mamou, M. L. Oelze, W. D. O'Brien, and J. F. Zachary, "Extended three-dimensional impedance map methods for identifying ultrasonic scattering sites," *J Acoust Soc Am*, vol. 123, no. 2, pp. 1195–1208, Feb. 2008, doi: 10.1121/1.2822658.

[50] V. C. Anderson, “Sound Scattering from a Fluid Sphere,” *The Journal of the Acoustical Society of America*, vol. 22, no. 4, pp. 426–431, Jul. 1950, doi: 10.1121/1.1906621.

[51] H. Azhari, “Appendix A: Typical Acoustic Properties of Tissues,” in *Basics of Biomedical Ultrasound for Engineers*, Hoboken, NJ, USA: John Wiley & Sons, Inc., 2010, pp. 313–314. doi: 10.1002/9780470561478.app1.

[52] L. Demi, B. E. Treeby, and M. D. Verweij, “Comparison between two different full-wave methods for the computation of nonlinear ultrasound fields in inhomogeneous and attenuating tissue,” in *2014 IEEE International Ultrasonics Symposium*, Chicago, IL, USA, Sep. 2014, pp. 1464–1467. doi: 10.1109/ULTSYM.2014.0362.

[53] A. Han *et al.*, “Noninvasive Diagnosis of Nonalcoholic Fatty Liver Disease and Quantification of Liver Fat with Radiofrequency Ultrasound Data Using One-dimensional Convolutional Neural Networks,” *Radiology*, vol. 295, no. 2, pp. 342–350, May 2020, doi: 10.1148/radiol.2020191160.

[54] R. S. C. Cobbold, *Foundations of biomedical ultrasound*. Oxford; New York: Oxford University Press, 2007.

[55] J. J. Faran, “Sound Scattering by Solid Cylinders and Spheres,” *The Journal of the Acoustical Society of America*, vol. 23, no. 4, pp. 405–418, Jul. 1951, doi: 10.1121/1.1906780.

[56] T. K. Stanton, “Sound scattering by cylinders of finite length. III. Deformed cylinders,” *The Journal of the Acoustical Society of America*, vol. 86, no. 2, pp. 691–705, Aug. 1989, doi: 10.1121/1.398193.

[57] J. McNew, R. Lavarello, and W. D. O’Brien, “Sound scattering from two concentric fluid spheres,” *The Journal of the Acoustical Society of America*, vol. 125, no. 1, pp. 1–4, Jan. 2009, doi: 10.1121/1.3035901.

[58] D. Savéry and G. Cloutier, “A point process approach to assess the frequency dependence of ultrasound backscattering by aggregating red blood cells,” *J Acoust Soc Am*, vol. 110, no. 6, pp. 3252–3262, Dec. 2001, doi: 10.1121/1.1419092.

[59] A. Han, R. Abuhabsah, J. P. Blue, S. Sarwate, and W. D. O'Brien, "Ultrasonic backscatter coefficient quantitative estimates from high-concentration Chinese Hamster Ovary cell pellet biophantoms," *J Acoust Soc Am*, vol. 130, no. 6, pp. 4139–4147, Dec. 2011, doi: 10.1121/1.3655879.

[60] A. Han, R. Abuhabsah, R. J. Miller, S. Sarwate, and W. D. O'Brien, "The measurement of ultrasound backscattering from cell pellet biophantoms and tumors ex vivo," *J Acoust Soc Am*, vol. 134, no. 1, pp. 686–693, Jul. 2013, doi: 10.1121/1.4807576.

[61] A. Han and W. D. O'Brien, "Structure Function Estimated From Histological Tissue Sections," *IEEE Trans Ultrason Ferroelectr Freq Control*, vol. 63, no. 9, pp. 1296–1305, Sep. 2016, doi: 10.1109/TUFFC.2016.2546851.

[62] M. F. Insana, R. F. Wagner, D. G. Brown, and T. J. Hall, "Describing small-scale structure in random media using pulse-echo ultrasound," *J Acoust Soc Am*, vol. 87, no. 1, pp. 179–192, Jan. 1990, doi: 10.1121/1.399283.

[63] M. F. Insana and D. G. Brown, "Acoustic scattering theory applied to soft biological tissues," in *Ultrasonic scattering in biological tissues*, K. K. Shung and G. E. Thieme, Eds. Boca Raton, FL: CRC Press, 1993, pp. 75–124.

[64] A. Han and W. O'Brien, "Structure function for high-concentration biophantoms of polydisperse scatterer sizes," *IEEE Trans Ultrason Ferroelectr Freq Control*, vol. 62, no. 2, pp. 303–318, Feb. 2015, doi: 10.1109/TUFFC.2014.006629.

[65] A. C. Luchies and M. L. Oelze, "Effects of the container on structure function with impedance map analysis of dense scattering media," *J Acoust Soc Am*, vol. 143, no. 4, p. 2172, Apr. 2018, doi: 10.1121/1.5031124.

[66] E. S. Wise, B. T. Cox, J. Jaros, and B. E. Treeby, "Representing arbitrary acoustic source and sensor distributions in Fourier collocation methods," *The Journal of the Acoustical Society of America*, vol. 146, no. 1, pp. 278–288, Jul. 2019, doi: 10.1121/1.5116132.